Magnetic Ordering of Dipolar Spin Ice in Moderate [111] Field

by

Brian Yee

A thesis
presented to the University of Waterloo
in fulfilment of the
thesis requirement for the degree of
Master of Science
in
Physics

Waterloo, Ontario, Canada, 2016

AUTHOR'S DECLARATION

I hereby declare that I am the sole author of this thesis. This is a true copy of the thesis, including any required final revisions, as accepted by my examiners.

I understand that my thesis may be made electronically available to the public.

ABSTRACT

This thesis explores the low temperature physics of the macroscopically degenerate system of dipolar spin ice in moderate fields applied along the [111] cubic axis. While most applications of field generically lift the macroscopic degeneracy, the [111] direction only partially removes this degeneracy leaving behind a large manifold of states known as dipolar kagome spin ice. Building on prior numerical sampling methods, we develop non-local statistical sampling techniques specifically tailored to the dipolar kagome spin ice regime, as well as considerations about system geometry to account for commensurabilities. We will find a long rage order sets in below $T \lesssim 0.1$ K between a range of fields of 0.02 T $\lesssim |\boldsymbol{B}| \lesssim 0.83$ K. This long range order will prove to be sensitive to perturbations and exist among a host of other metastable states extremely close in energy. A final discussion on future work and the possible need for clustering algorithms or study of other related systems concludes this work.

ACKNOWLEDGEMENTS

Glück ist Liebe, nichts anderes.
Wer lieben kann, ist glücklich.
— Herman Hesse

Für Berry.

CONTENTS

LIST OF FIGURES

LIST OF TABLES

LIST OF ABBREVIATIONS

DKA   Dipolar kagome ising antiferromagnet

DKI   Dipolar kagome ice

DKSI   Dipolar kagome spin ice

DSI   Dipolar spin ice

MCS   Monte carlo sweeps

MFT   Mean field theory

NNSI   Nearest neighbour spin ice

PBC   Periodic boundary condition

PKP   Perpendicular kagome plane

SKP   Slanted kagome plane

Part I

INTRODUCTION

The Ising model, first conceived in 1920 has become perhaps the quintessential model in the study of magnetism. Recently, great interest has been drawn to the Ising model when placed on various lattices which exploit its simple rules to locally *frustrate* the interactions. In this part, we outline one of the most exotic cases of these frustrated Ising models known as *spin ice*. We map out the original theoretical motivation and subsequent development of the model in real materials. Fascinatingly, we will find the microscopically motivated Hamiltonian reduces into a set of states predicted by the most simplistic model, due to a sophisticated partial cancellation of the dipolar interactions present. From these set of states, the selection of a minimal energy configuration is predicted at very low temperatures, using numerical techniques left to be described in Chap. 3. We will discuss why this low temperature configuration has eluded experimentalists for nearly a decade, and the recent developments which have recast the question of low temperature ordering. Finally, we will state the primary research question of this work and briefly outline the structure of this thesis.

INTRODUCTION

1.1 FRUSTRATION

1.1.1 *Geometric Frustration*

In the context of magnetism, geometric frustration arises in situations where local geometric constraints preclude the ability to simultaneously satisfy all pairwise interactions for a given system [1]. To demonstrate this concept, consider two systems each with Ising spins located on the vertex of a given plaquette. Each spin interacts via a pairwise Ising antiferromagnetic interaction with its nearest-neighbour given by the simple Hamiltonian

$$H = J_o \sum_{\langle ij \rangle} \sigma_i \sigma_j \tag{1.1}$$

where σ_i represents an Ising spin which can take the value of $\{-1, +1\}$ and $J_o > 0$. For this system, the energy is minimized when all spins are *anti*-aligned with their nearest-neighbours. As shown in Fig. 1.1(a), for a square plaquette, all pairwise interactions of the Hamiltonian can be simultaneously satisfied. Contrarily, for a triangular plaquette if two spins satisfy a pairwise interaction, a third spin can never be chosen which satisfies every interaction with its neighbours.

(a)   (b)
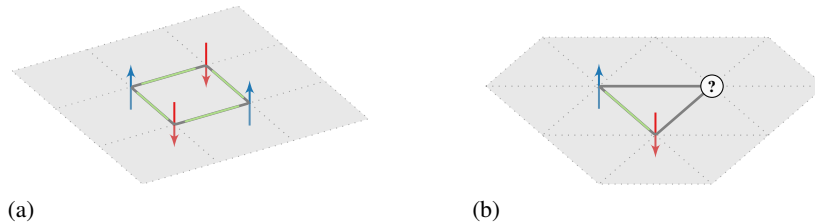
Figure 1.1: Examples of Ising antiferromagnets: (a) an unfrustrated square plaquette, (b) a frustrated triangular plaquette. Green bonds indicate satisfied pairwise antiferromagnetic interactions, while a question mark resides at a site which cannot simultaneously satisfy both nearest-neighbour interactions.

1.1.2 *Frustration in Different Dimensions*

The concept of frustration can be generalized from simple plaquette configurations to various two dimensional lattices which display the phenomenon. Perhaps unsurprisingly, systems with frustrated/unfrustrated plaquettes can be combined to create other frustrated/unfrustrated lattices. These plaquettes can be edge-sharing as in the square

(a)   (b)

(c)
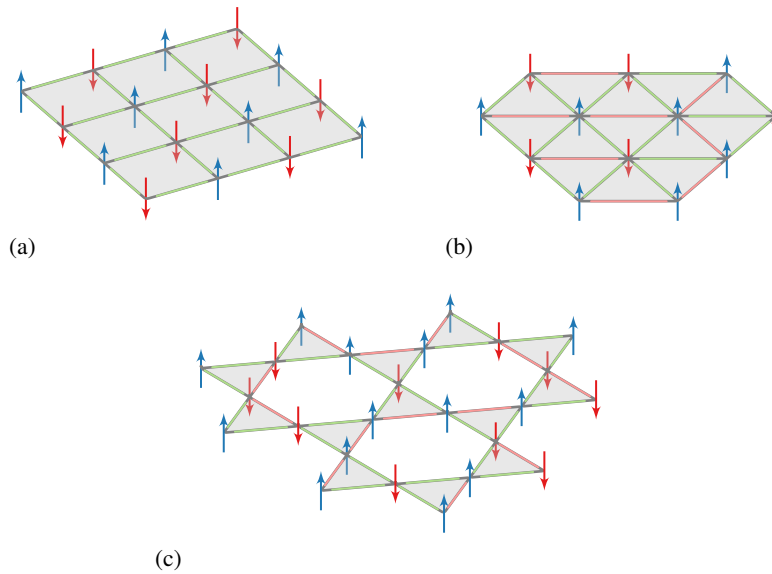
Figure 1.2: Examples of 2D Ising (a) unfrustrated, (b)/(c) frustrated antiferromagnets. Green bonds indicate satisfied pairwise antiferromagnetic interactions, while red bonds indicate unsatisfied pairwise interactions. While two states trivially satisfy all interactions for the square plaquette (a), there exists no simple set of solutions for the triangular lattice (b) and the *kagome* lattice (c).

and triangular lattices shown in Fig. 1.2 (a), (b) or corner-sharing as in the *kagome* lattice shown in Fig. 1.2 (c). By inspection, only two ground states exist for the antiferromagnetic Ising model on a square lattice. When looking at the frustrated cases of Fig. 1.2 it is hard to construct an easily countable set of ground states. Indeed, due to the multiple ways a system can arrange the frustrated bonds a *macroscopic degeneracy* of the ground state is present [1]. That is, in the thermodynamic limit, configurations of spins which minimize the energy of the system are not restricted to only global symmetry. Frustration can also manifest in three dimensions, by generalizing the frustrated triangle plaquette in Fig. 1.1 to a three dimensional tetrahedron analogue, which is six
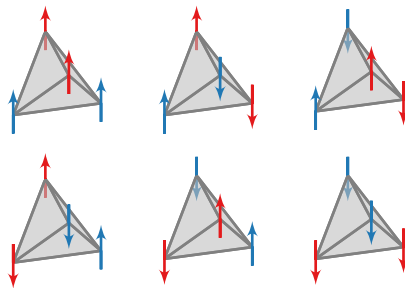
Figure 1.3: Ground state degeneracy of a tetrahedron with Ising moments pointing along the global $\hat{z}$ direction. This degeneracy demonstrates the tetrahedron is an excellent building block for 3D frustrated lattices as shown in Fig. 1.4.

(a)   (b)
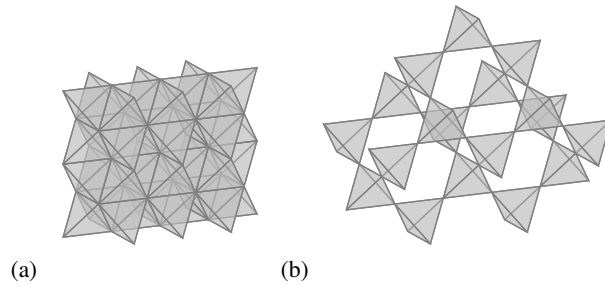
Figure 1.4: Networks of edge sharing and corner-sharing tetrahedra forming (a) the face centered cubic lattice and (b) the pyrochlore lattice. Each can be though of as the three dimensional analogues of their two dimensional frustrated counter parts of (a) the triangular lattice and (b) the kagome lattice.

fold degenerate for an antiferromagnetic Ising interaction as shown in Fig. 1.3. Just as two dimensional corner- and edge-sharing triangles can form frustrated lattices, corner and vertex sharing tetrahedra can form frustrated three dimensional lattices, as shown in Fig. 1.4. The frustrated face centered cubic lattice can be thought of as an edge sharing network of tetrahedra, a generalization of the triangular lattice in two dimensions. Similarly, the frustrated *pyrochlore* lattice – of primary concern in this thesis – can be thought of as a vertex sharing network of tetrahedra, a generalization of the kagome lattice.

1.1.3 *Physical Manifestations of Frustration*

While frustration may sound like an exotic construct, it is present within one of the most ordinary substances of everyday life – solid water ice – more commonly referred to as ice. Nearly a century ago, the structural properties of ice in regular atmospheric conditions were still a matter of debate [2]. A paper published by Barnes unequivocally demonstrated that in regular atmospheric conditions the freezing which occurs, results in hexagonal planar sheets of oxygen atoms forming the structure now referred to as I_h [2]. Shortly after, Bernal and Fowler proposed a theory of crystalline water, defining a set of "ice-rules" dictating where the hydrogen atoms are placed in relation to the oxygen atoms [3]. The ice-rules state that:

- one hydrogen atom exists between every oxygen pair

- each oxygen atom has two nearby hydrogen atoms placed such that the molecular structure of H_2O is preserved

To illustrate this, Fig. 1.5 shows a portion of the I_h lattice obeying the ice-rules. While many variations in the lattice structure of crystalline ice frozen in different atmospheric conditions exist today each one adheres to these ice rules. Due to the covalent bonds of each H_2O molecule, each oxygen atom has two nearby protons, and two protons located farther away. The amount of ways these ice-rules can be satisfied results in a property known as *residual* or *zero-point* entropy.
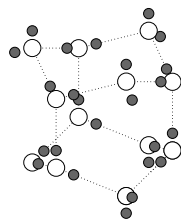
Figure 1.5: A portion of the I_h showing an arrangement of H_2O molecules obeying the ice rules. White and black dots represent oxygen atoms and hydrogen atoms respectively, while dotted lines represent bonds along O-O pair. By rule (1), an O-O pair can only have one hydrogen atom present between each oxygen atom.

In statistical mechanics, entropy is defined as

$$S \equiv k_B \ln(W), \tag{1.2}$$

where k_B is the Boltzmann constant and the multiplicity W is defined as the number of distinct micro-states which can describe a given macro-state. At zero temperature, the system can be found in the ground state configuration. Usually, the ground state configuration is one of a set of multiple ground states related by global symmetry. Due to this restriction of ground states, in the thermodynamic limit as the temperature $T \to 0$, the entropy also approaches zero in accordance with the third law of thermodynamics. However should the multiplicity grow exponentially as $W = W_o^N$, then the entropy

$$S = k_B \ln(W_o^N) = N k_B \ln(W_o), \tag{1.3}$$

does not approach zero in the thermodynamic limit as $T \to 0$, seemingly violating the third law of thermodynamics. Such systems are said to have a residual entropy. The residual entropy inherent in the proton disorder of ice was measured in 1933 [4], and explained two years later by Linus Pauling [5] through a beautifully succinct argument that goes as follows:

Given N water molecules obeying the ice-rules, each water molecule has 6 possible orientations with 2 nearby protons satisfying rule (2). Consider the bond formed by 2 water molecules joined in a tetrahedral fashion as in ice. To satisfy rule (1), each molecule is required to orient itself such that only 1 proton exists between the molecules of which (3/6) possibilities exist. The probability each molecule orients itself correctly independently is thus $(1/2)^2 = (1/4)$. This (1/4) probability is consistent with any of the 6 orientations leading to an expected degeneracy of 6/4 for each O-O pair. The residual entropy of the state is then obtained from the expected degeneracy of the system $W = (6/4)^{N/2}$ where $N/2$ is introduced to avoid double counting. Using Eq. 1.3 the residual entropy is then expected to be $S = k_B(N/2) \ln(3/2)$.

1.2 NEAREST-NEIGHBOUR SPIN ICE

In 1956, Anderson studied a model of ferrites, with Ising moments pointing along the global $\hat{z}$ direction on the pyrochlore lattice [6]. Anderson showed this model is minimized when each tetrahedron has two spins pointing upwards or downwards. However,

the choice of Ising spins pointing along $\hat{z}$ is somewhat arbitrary as the cubic symmetry equally allows the spins to point along the $\hat{y}$ or $\hat{z}$ directions [7, 8]. With no physical motivation as to why one particular direction should be preferential, the model remained purely theoretical for 40 years.

In 1997, Harris *et al.* made experimental contact with Anderson's model – demonstrating that ice-like behaviour could describe the magnetization and neutron scattering in the rare earth magnet holmium titanate ($Ho_2Ti_2O_7$) [9]. Harris *et al.* presented an Ising model on the pyrochlore lattice with spins pointing along the local [111] directions interacting via a *ferromagnetic* interaction. The local [111] directions coincide with each spin pointing directly into or out of a tetrahedron from each vertex. In a cubic geometry, these orientations are given by

$$S_1 = \frac{\sigma}{\sqrt{3}} \left(\hat{x} + \hat{y} + \hat{z} \right) \qquad\qquad S_3 = \frac{\sigma}{\sqrt{3}} \left(-\hat{x} + \hat{y} - \hat{z} \right)$$
$$S_2 = \frac{\sigma}{\sqrt{3}} \left(\hat{x} - \hat{y} - \hat{z} \right) \qquad\qquad S_4 = \frac{\sigma}{\sqrt{3}} \left(-\hat{x} - \hat{y} + \hat{z} \right) \qquad (1.4)$$

where $\sigma = \pm 1$. Realizing this model was mappable to the proton disorder in water ice, Harris *et al.* named the model *spin ice*. The frustration in spin ice was especially peculiar, as one would generally expect a ferromagnetic Ising model with a Hamiltonian as in Eq. (1) with an exchange constant of $J_o < 0$. In spin ice, the dot product of the easy axis moments results in an interaction with an additional prefactor $(-1/3)$ requiring $J_o > 0$ to induce frustration creating an effectively antiferromagnetic model. Similarly to Anderson's model this system is minimized when each tetrahedra has 2 spins pointing inward and 2 spins pointing outward. These rules which minimize the energy of spin ice, are equivalent to the ice-rules which dictate the proton disorder in regular water ice provided:

- the water molecules are joined in a fashion such that the midpoint of O-O pairs form the pyrochlore lattice crystal structure of the rare earth titanates

- the local "2-near" and "2-far" ice-rules governing proton arrangement are replaced by a local "2-in" and "2-out" ice-rule governing how local magnetic moments point towards their respective tetrahedra

This mapping is explicitly shown in Fig. 1.6.

1.3 DIPOLAR SPIN ICE

It is well known that the rare-earth cations carry large magnetic moments and relatively small super-exchange factors [11]. First mentioned by Siddharthan *et al.*, $Dy_2Ti_2O_7$ and $Ho_2Ti_2O_7$ have non-magnetic Ti^{4+} and O^{2-} ions leaving the rare earth ion to carry a large magnetic moment from an unfilled f-electron shell [11]. Thus, in the rare earth titanates one expects the large dipolar moment to result in a non-negligble dipolar mo-
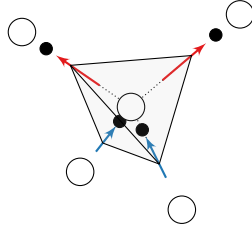
Figure 1.6: The mapping between the crystalline water ice-rules and spin ice ice-rules, with white and black dots denoting the oxygen and hydrogen atoms respectively. Spins located at the midpoint O-O pairs in a tetrahedral fashion either directly into or out of a tetrahedron. The 2-near and 2-far ice-rule for protons are replaced by a 2-in 2-out rule for how spins point on the tetrahedron.

ment when compared to the super-exchange constant. Including this dipolar term, the dipolar spin ice Hamiltonian in an applied magnetic field is

$$H = \frac{J}{3} \sum_{\langle ij \rangle} \sigma_i \sigma_j + D r_{nn}^3 \sum_{i>j} \left(\frac{\hat{z}_i \cdot \hat{z}_j}{|\boldsymbol{r}_{ij}|^3} - \frac{\left(\hat{z}_i \cdot \boldsymbol{r}_{ij} \right) \left(\hat{z}_j \cdot \boldsymbol{r}_{ij} \right)}{|\boldsymbol{r}_{ij}|^5} \right) \sigma_i \sigma_j - \mu \sum_i \left(\hat{z} \cdot \boldsymbol{B} \right) \sigma_i \quad (1.5)$$

Where $\boldsymbol{B}$ is an applied field and the strength of the dipolar moment D is fixed by the dipolar moment $\mu \sim 10\mu_B$

$$D = \left(\frac{\mu_0}{4\pi} \right) \frac{\mu^2}{r_{nn}^3} \sim 1.41 \text{ K} \quad (1.6)$$

and the nearest-neighbour distance r_{nn} [8, 12, 13]. The factor of $(5/3)$ is a property of the pyrochlore lattice geometry where $(\boldsymbol{S}_i \cdot \boldsymbol{r}_{ij})(\boldsymbol{S}_j \cdot \boldsymbol{r}_{ij}) = -2/3$ and, as mentioned previously, $\hat{z}_i \cdot \hat{z}_j = -1/3$ for nearest-neighbour interactions. A subsequent fitting of the remaining unknown parameter J in the Hamiltonian was performed by Hertog and Gingras using experimental data to determine a value of $J = -3.72$ K for $Dy_2Ti_2O_7$ [12].

To consider how the interplay of these two values leads to frustration, it is beneficial to consider an effective interaction

$$J_{eff} = J_{nn} + D_{nn} \quad (1.7)$$

for quantifying behaviour at the level of nearest-neighbours [12]. To obtain an effective nearest model which induces frustration on the pyrochlore lattice we than require $J_{nn} + D_{nn} > 0$. Both $Dy_2Ti_2O_7$ and $Ho_2Ti_2O_7$ fulfil this condition with $J_{eff} = 1.11$ K and $J_{eff} = 1.83$ K, respectively [14].

Beyond the nearest-neighbour level remains dipolar interactions decaying as $1/r^3$ making them a *long-ranged* interaction. This long-ranged nature means that the dipole interactions are *conditionally* convergent and an imposed cutoff of their interactions results in spurious correlations [15]. Furthermore, given the large dipolar interactions, one might expect that the complicated geometrical dependence of so many remaining dipolar interactions to be summed would be sufficiently perturbative to lift the degeneracy of

the ice-manifold destroying the behaviour completely. Hertog and Gingras properly handled these interactions using the well-established Ewald method [16], which splits the conditionally convergent sum into two absolutely and rapidly converging sums in direct and reciprocal space. Using Monte Carlo simulations with local spin flip dynamics and integrating the specific heat[1], their results showed Pauling's entropy was still recovered [12].This retainment of Pauling's entropy occurred due to many partial cancellations of the dipolar interaction causing an effective self-screening [12]. This self-screening behaviour of the dipoles would be later quantified more formally and given the name of *projective equivalence* [17].

The projective equivalence in dipolar spin ice (DSI) results in the same spin-ice manifold at moderate temperatures of $T \lesssim (J_{nn} + D_{nn})$ described by the nearest-neighbour spin ice (NNSI) put forward by Harris *et al.*. Additional residual interactions present in DSI make the previously degenerate ice manifold *quasi*-degenerate with minute differences between ice-states due to the dipolar interactions. Minimizing this remaining set of dipolar interactions requires the development of new statistical sampling techniques – a point so important to this thesis it is discussed in explicit detail in Chapt. 3. For now, we acknowledge that these special sampling techniques were used in a numerical study by Melko *et al.* to identify an ordered ground state from the quasi-degenerate ice-manifold [13]. This ordering is signified by a sharp peak in the specific heat at $T \sim 0.2$ K corresponding to a removal of Pauling's entropy. Until recently, experimental evidence of this ordered state has eluded experimentalists most likely due to the extreme difficulty in equilibrating spin-ice systems at low temperatures.

1.3.1 *Dynamics & Evidence of Ordering*

The spin relaxation time of a system is a measure of the time for a system to return to equilibrium after a disturbance. The investigation of low temperature physics requires a feasible relaxation time for probing thermodynamic quantities of interest. The spin relaxation time of $Dy_2Ti_2O_7$ can be decomposed into three regions [18] : an Ahrennious process at high temperature, a relaxation plateau of lower temperatures and a final faster than exponential increase for $T \lesssim 1$ K [19, 20]. Of special concern on the nature of ordering in DSI is the behaviour for $T \lesssim 1$ K where the transition studied by Melko *et al.* is predicted to exist [13]. Given the faster than exponential increase in relaxation time, a vicious slow down of the dynamics occurs in DSI resulting in very long equilibration timescales for experimentalists. Attempts made to address these long timescales and capture the low-temperature behaviour of $Dy_2Ti_2O_7$ down to $T \sim 0.3$ K were made but failed to see any signature of the beginning of a transition [10, 21–24]. Recently, the conclusions of the low-temperature physical properties drawn from these experiments have been re-evaluated in light of new data [25]. Experiments performed carefully considering the flow of heat through samples found an additional upturn in the specific heat not previously seen providing direct evidence of the removal of the residual entropy in $Dy_2Ti_2O_7$ [25]. Possible theories on the removal of this entropy have been put forward

---

1 The derivation and details of which will be motivated in Chapter 3

attributing it to either quantum effects begining to manifest [26] or the beginning of a transition into an ordered state [25]. Additionally, recent results suggest that among the possible theories put forward random disorder caused by an unexpected refrustration induced by small nearest neighbour exchange is the most reasonable explanation of the calorimetric data [27].

To better understand the nature of dipolar ordering in spin ice, it is perhaps beneficial to consider alternate cases to help highlight specific aspects of the complex ordering. One way to achieve this is to consider the application of a magnetic field where one can assess ordering on a sub-manifold of states obeying the ice-rules with additional Zeeman considerations. This thesis aims to address the special case of dipolar ordering when a moderate field is applied directly along a direction corresponding to one of the four directions of Ising spin ice moments written in Eq.1.4. More succinctly: what is the ground state and transition of DSI in a field of moderate strength along the [111] cubic axis?

1.4 OUTLINE OF THESIS

This concludes the Introduction of this work, aimed to aid the reader in developing a working understanding of the modern state of DSI in zero field. The remaining portion of this work will be divided into four chapters. Chapter 2 will introduce DSI in the context of magnetic fields and introduce their respective ground states in various high symmetry fields. The primary focus of Chapter 2 is to build a physically oriented understanding of DSI in field, while the numerical techniques required to investigate them are outlined in significant detail in Chapter 3. Chapter 4 will present the results of applying the methods presented in Chapter 3 on the dipolar spin ice Hamiltonian with a moderate field applied along the [111] axis. In an attempt to understand the ordering behaviour at the most basic level, we take the model of DSI given by Eq.1.5 leaving additional further neighbour exchange corrections to future work. Other possible avenues of future work are discussed in Chapter 5.

Part II

PREVIOUSLY STUDIED DIPOLAR MODELS & METHODS

In this part, we review the numerical techniques used to study DSI and the resulting thermodynamic properties. We begin by reviewing the current state of knowledge for DSI in high symmetry fields, reviewing previous studies and their interesting experimental applications. Of equal interest theoretically and experimentally, we delve into details of the special case of applied field along the [111] cubic axis. We discuss the case of moderate field which partially lifts the macroscopic degeneracy resulting for an intermediate state occurring before complete saturation in high fields. This [111] intermediate state will be related to two dimensional kagome systems, which we will review to help equip ourselves to understand the full three dimensional model.

Once these states have been physically motivated, we will discuss the numerical *Monte Carlo* techniques used to explore these systems and quantify their respective ground states. While they are all related by the concept of quasi-zero modes, more sophisticated techniques will be developed and subsequently customized to best account for thermally relevant low temperature fluctuations. The concept of metastability and commensurability will be visited, as well as the correct handling of long range interactions which cannot be trivially truncated in direct space. Finally, we derive a set of self-consistent *mean field* equations which will support the results from Monte Carlo simulations.

DIPOLAR ORDERING IN ICE SYSTEMS

2.1 DIPOLAR SPIN ICE IN ZERO FIELD

Long range ordering of dipoles on the pyrochlore lattice was first studied by Melko *et al.* for DSI in zero field [13]. Building on the single spin flip Monte Carlo simulations of Hertog and Gingras, an additional *loop* move[1] was added to aid in sampling the ice state manifold. The loop move proved to be extremely effective sampling method, revealing a sharp feature in the specific heat indicative of a first order phase transition into an ordered state [13, 14, 28]. The ordered state found has an 8-site magnetic unit cell, commensurate with the cubic unit cell state is shown in Fig. 2.1 . The state can be viewed as alternating antiparallel stacked chains of spins along any given cubic axis, resulting in a zero magnetic moment. Twelve symmetric states can be generated through the reversal of chains and the six tetrahedral edges the chains can manifest upon. The corresponding wave vector describing the state is given by $(0, 0, 2\pi/a)$ in agreement with mean field theory calculations presented by Gingras *et al.* [13–15, 28]. This state which we hereafter refer to as the [001] state, demonstrated the need for sophisticated numerical techniques when studying DSI at low temperatures.
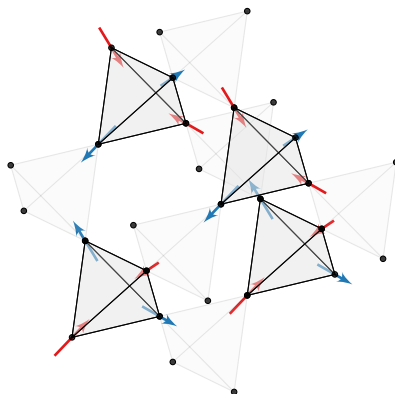
Figure 2.1: The [001] ground state of DSI in zero field commensurate with the cubic unit cell indicated by shaded in tetrahedra. Lightly shaded peripheral tetrahedra have been added to help demonstrate how the spin arrangement arranges itself on the pyrochlore lattice. Red and blue colours have been added to aid in seeing the antiferromagnetically coupled chains of parallel spins.

---

1 An outline of the single spin flip and loop method will be discussed in depth in Chapter 3

(a)

(b)

Figure 2.2: The (a) $q = 0$ state and (b) $q = X$ commensurate with the cubic unit cell indicated by shaded in tetrahedra. Lightly shaded peripheral tetrahedra have been added to help demonstrate how the spin arrangement arranges itself on the pyrochlore lattice. Purple and green highlighted regions represent α-chains and β-chains, respectively. Red and blue colours have been added to spins to aid in seeing the antiferromagnetically coupled chains of parallel spins. A green arrow has been added to show the direction of the applied magnetic field.

2.2 DIPOLAR SPIN ICE: IN MAGNETIC FIELDS

2.2.1 *Dipolar Spin Ice:* [001] *Field*

The simplest ground state one can consider for DSI in a field, is the saturated $q = 0$ state for the [001] field. All spins couple with the field equally and are pinned for a sufficiently large field, as shown in Fig. 2.2(a). While this ground state can be trivially predicted and it has been observed experimentally via neutron diffraction techniques in $Ho_2Ti_2O_7$ [29], the mechanism by which the transition occurs remains non-trivial. Originally, the mechanism was predicted by Harris *et al.* to be of the first order type [7]. However, it was later discovered by Jaubert *et al.* that, through the use of non-local numerical techniques introduced by Melko *et al.* the mechanism of transition is instead that of a 3D Kastelyn transition [30, 31].

2.2.2 *Dipolar Spin Ice:* [112] *Field*

Another case where the system selects the $q = 0$ state occurs without the all spins coupling to the field. An application of a large magnetic field along the [112] direction pins three spins on a tetrahedra into a 2-out 1-in configuration creating an internal field acting on the remaining fourth spin [32]. To satisfy the 2-in 2-out ice-rules the remaining spin points inwards selecting the $q = 0$ state. Simulations of $Dy_2Ti_2O_7$ by Ruff *et al.* in

the case of infinite field predict a broad Schottky like feature in the specific heat near ~ 1.7 K [32].

Another interesting case to consider is when the [112] field is slightly tilted towards the [110] cubic axis. For a given tilt angle the magnetic field can be tuned such that it exactly cancels out the internal field, produced by the three pinned spins. The fourth remaining spin, now independent of the internal field acts as a free Ising spin providing a physical realization of a dipolar Ising FCC model [32]. One can now predict the ordering of these dipoles by examining the previously studied dipolar FCC Heisenberg model which has a ferromagnetic ground state [32–34]. An excellent choice for a candidate ground state for the Ising model is then ferromagnetic, with the magnetization direction given by the axis of the freed spins along the [$\bar{1}\bar{1}1$] direction, ordering at $T_c \sim 0.35$ K. Simulations of DSI in tilted field, confirmed the ferromagnetic ordering although the ordering occurred for $T_c \sim 0.65$ K [32]. This large discrepancy between the critical temperatures of the FCC dipolar ising model and DSI in tilted [112] field was resolved through a third nearest-neighbour exchange interaction of $J_3 = -0.022$ K [32]. Upon applying this correction, the simulated DSI specific heat peak was found to occur in better agreement with the dipolar FCC ising model, ordering at $T_c \sim 0.35$ K [18]. An interesting observation drawn from this correction is its existence in the range of -0.03 K $< J_3 < -0.01$ K, which has been shown to help explain the paramagnetic zone boundary for neutron scattering experiments of $Dy_2Ti_2O_7$ [32, 35].

This lead to the proposal that given sufficient accuracy in the alignment of an applied magnetic field, experiments of a tilted [112] field could provide measurements to fit the J_3 interaction with a very high precision [32]. Shortly after, Sato *et al.* presented experimental results using a magnetic field applied along the [112] to pin the spins and an additional local [111] field to cancel the internal field [36]. Enabled by these results Yavors'kii *et al.* refined the DSI model with up to third nearest-neighbour interactions [37] as the most accurate fitting at its time. In light of the upturn in specific heat of $Dy_2Ti_2O_7$ as mentioned in the Chapt 1, these results have since had to be revisited to accommodate new experimental results [27, 38].

2.2.3 *Dipolar Spin Ice:* [110]

The pyrochlore lattice can be thought of as four FCC sublattices, each defined by selecting spins with the same local [111] moments. Similar to the decoupling of one spin which occurs in the [112] case, the [110] results in a decoupling of spins on two FCC sublattices. In the limit of high field the spins which couple to the field become pinned forming chains of alternating inwardly and outwardly pointing spins referred to as α-chains, shown in Fig. 2.2. b. To satisfy the ice rules, the remaining decoupled spins again form chains of alternating inwardly and outwardly point spins referred to as β-chains, also shown in Fig. 2.2. b. Due to the remaining freedom of the β-chains, the ordering of the system can be understood by considering their minimal energy configurations. Based on the antiferromagneticly stacked chain arrangement present in the zero field case, a good candidate ground state for the β-chains to order would then be antifer-

romagnetic with their nearest-neighbour β-chains. This state, first put forward by Harris *et al.* in the experimental context of neutron scattering results on $Ho_2Ti_2O_7$ is referred to as the $q = X$ state [9].

Monte Carlo simulations of DSI in [110] have since established the $q = X$ state to be the ground state transitioning into the state via a one- to three-dimensional cross over from the paramagnetic regime [32, 39]. Unfortunately, while Monte Carlo simulations have provided excellent evidence for the $q = X$ state as the ground state, quantitative experimental evidence of this ordering is still lacking [29, 40]. One argument for why it has yet to be observed is the requirement of an extremely precise alignment of the magnetic field to prevent any coupling with the β-spins which may destroy the long range order [14, 40].

So far we have been able to motivate the ground states of DSI in [001], and [001] applied magnetic fields using the knowledge of the zero field case and for the [112] case, a related Heisenberg system. The remainder of this work is concerned within the context of the last high symmetry case field yet to be discussed – ordering of DSI with the field applied along the [111] cubic axis. We will find that while the ground state can still be predicted for large [111] fields, no simple argument will exist for the case of moderate field strength.

2.2.4 *Dipolar Spin Ice:* [111] *Field*

The special case of the [111] field is best illustrated by examining the magnetization curves of various strengths of magnetic field. At low temperature and various field for each case thus far, the magnetization of a system gradually increases towards a predicted magnetization known from each ground state [36, 41–43]. Interestingly, this is not the case for the [111] field, where the low temperature magnetizaton develops a plateau for intermediate field strengths [41–45]. This intermediate state which the plateau describes, is referred to as *kagome spin ice* for reasons which will become readily clear. The statics and dynamics of this plateau, was investigated theoretically by Moessner and collobarators [46, 47] whose discussion can be distilled as follows.

As shown in Fig. 2.3 the application of a [111] field decomposes the pyrochlore lattice into layers with alternating Zeeman potentials. Spins residing on the triangular sites with an Ising moment parallel with the magnetic field, experiencing a projection onto the magnetic field of $\sigma = \pm 1$, while spins residing on kagome planes experience a projection of $\sigma = \pm 1/3$. Since all spins couple to the field, the high field plateau can be described by a 3-in/1-out configuration for every spin, where the magnetization is given by

$$|m| = -\mu \sum_i (\hat{z} \cdot \boldsymbol{B}) \sigma_i$$

$$= \frac{\mu}{4} \left(\frac{1}{\sqrt{3}} \right)^2 \left([111] + [\bar{1}11] + [1\bar{1}1] + [11\bar{1}] \right) \cdot [111] = \frac{1}{2}\mu \qquad (2.1)$$

Where $\mu \approx 10\mu_B$ is the magnetic moment of the dysprosium required to measure it in the appropriate experimental units of μ_B/Dy^{3+}. As the applied field is lowered and

| (a) | (b) |
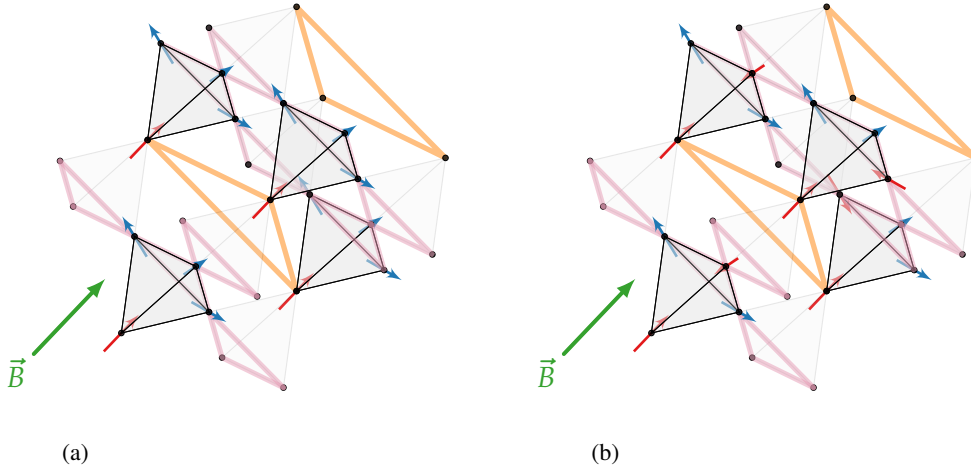
Figure 2.3: Spin configurations of the two magnetization plateaus for DSI in field, with (a) 3-in/1-out saturated case and (b) kagome ice. The pyrochlore lattice is decomposed into sets of interleaved (orange) triangular and (pink) kagome planes. The kagome ice and 3-in/1-out state differ by the selection of a minority spin which points anti-parallel to the field indicated by red spins on the kagome plane. A green arrow indicating the direction of applied field and lightly shaded peripheral tetrahedra have been added to better understand how the spins arrange themselves in relation to the pyrochlore lattice.

the Zeeman couplings are reduced, the super-exchange energies begin to compete with the Zeeman energies. Of the six possible 2-in 2-out configurations possible for the ice-rules, three configurations correspond to a configuration with the triangular spin aligned with the field. Because the triangular spin projects fully onto the field, these three configurations are energetically favourable – that is, the triangular spins get pinned at low temperatures before the kagome spins. Thus, from the 3-in/1-out configuration, a *minority* spin from the kagome plane is chosen from each tetrahedron to oppose the field to obey a 2-in 2-out configuration, while the remaining *majority* spins continue to satisfy the ice rules while aligning with the field as much as the Ising anisotropy will allow. The theoretical value of the intermediate magnetization plateau can than be calculated as

$$|m| = -\mu \sum_i (\hat{z} \cdot \boldsymbol{B}) \, \sigma_i$$

$$= \frac{\mu}{4} \left(\frac{1}{\sqrt{3}} \right)^2 \left([111] + [\bar{1}11] + [1\bar{1}1] - [11\bar{1}] \right) \cdot [111] = \frac{1}{3} \qquad (2.2)$$

The thermal fluctuations of this stabilized regime are determined by the majority and minority spins on the layered kagome lattices. The arrangement of these majority and minority spins can be mapped to a hexagon dimer model with the well known entropy of $S \approx 0.16153 k_B$ per site [46]. Since each triangle on the kagome lattice can be defined

given only two sites, the system retains a residual entropy half that of the dimer model giving

$$S \approx 0.08077 k_B \tag{2.3}$$

demonstrating the existence of a residual entropy in the stabilized regime. Given a residual entropy remains to be removed, one can consider the role of additional dipolar interactions in this state creating a *dipolar kagome spin ice* (DKSI) model. The subject of this thesis, is the systematic search of this DKSI model, for the ordered state that removes this residual entropy.

Recently, the transition from kagome spin ice to the 3-in/1-out state has attracted great interest due to the existence of a critical point, exhibiting a liquid-gas like transition [45].This transition is most naturally thought of in the *dumbbell convention* where the dipoles on the pyrochlore lattice are lengthened to form dumbbells with equal and opposite charges on either end, as shown in Fig. 2.4. These dumbbell charges convene at the center of each tetrahedron forming a diamond lattice of charge values Q, with values $Q = \{0, \pm 2, \pm 4\}$. These charges interact via the Coulombic potential

$$Q = \begin{cases} \frac{\mu_0}{4\pi} \frac{Q_{\alpha\beta}}{r_{\alpha\beta}}, & \alpha = \beta \\ \frac{1}{2}\nu_0 Q_{\alpha}^2, & \alpha \neq \beta \end{cases} \tag{2.4}$$

where $Q_{\alpha\beta}$ denotes the charge imbalances for two sites separated by the radius $r_{\alpha\beta}$ and the value ν_0 corresponds to a finite self-energy required to reproduce the effective nearest-neighbour interactions [48]. In this model, an ice state where all dumbbells obey a 2-in 2-out rule corresponds to a charge of $Q = 0$ everywhere. Given a local dipolar excitation corresponding to a dumbbell flip, the two adjacent tetrahedra experience an equal and opposite imbalance of charges. These charge imbalances can be removed further from each other by restoring the ice rules of the defective tetrahedra locally, while displacing the charge imbalance to an adjacent tetrahedron through single spin flips, as shown in Fig. 2.5. Using Eq. 2.4, one finds a *finite* cost of creating and separating two charges in the limit of $r_{\alpha\beta} \to \infty$ [48]. This property known as *deconfiment*,

(a)   (b)
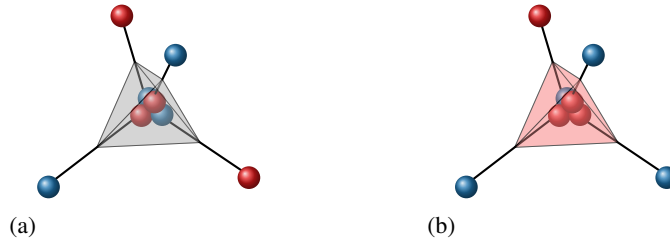
Figure 2.4: The dumbbell convention of DSI, point dipoles on the lattice are elongated and given equal and opposite charges represented by red and blue spheres. These charges can be summed and vanish for ice rule obeying states as in (a). If an imbalance is present, the charge interacts via a Coulomb wise potential with other charge imbalances – in effect as an emergent magnetic monopole.
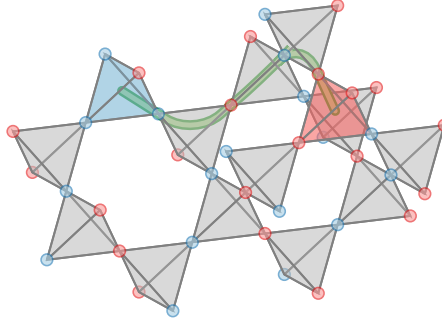
Figure 2.5: An ice-state represented by inward and outward spins given by red and blue points respectively, with one elementary excitation. The excitation results in two monopoles represented by red and blue tetrahedra which can be separated indefinitely by flipping a tail of spins represented by the green tail connecting each monopole. The cost of creating this tail is finite giving the monopoles the property of deconfinement.

demonstrates that these charge imbalances are true elementary excitations of the system which interact via a Coulombic potential *i.e.* monopoles! It is important to note that these monopoles are an *emergent* quasi-particles of spin ice – not the same monopoles predicted by Dirac which are *elementary* particles. However, this caveat should not deter the reader from the excitement that these spin-ice monopoles are still examples of high-dimensional fractionalization [48].

In this new view of monopole dynamics, the 3-in/1-out state becomes a monopole crystal composed of alternating layers of monopoles, while the kagome spin ice regime exists with a sparse population of monopoles. Thus the liquid-gas transition can be viewed as the transition between states of high and low monopole density. The specifics of this transition at the critical endpoint have been numerically identified by Hamp *et al.* to fall within the three-dimensional Ising universality class [49].

Given all this knowledge of kagome ice plateaus and low temperature DSI in various applied fields, the reader may perhaps find it surprising than that the ground state of DKSI still remained unknown when this work was initiated. In part, the reason for this is that for all other cases of applied field the degeneracy is completely lifted, enabling one to construct arguments for what the ground states should likely be and where to look, *e.g.* the relation between the dipolar FCC Heisenberg model and DSI in a tilted [112] field. As shown priorly in DKSI, a macroscopic degeneracy remains within the kagome planes creating a large set of potential configurations for the ground state to reside in, making the identification of a potential ground state significantly more difficult. Since each of the multiple kagome planes are macroscopically degenerate system individually; the study of ordering in single ice-like kagome systems has been the primary source of investigative efforts thus far. Before proceeding to investigate the case of DKSI, a review of these single two-dimensional layer systems will prove to be extremely valuable if not necessary to help guide our understanding of our system.
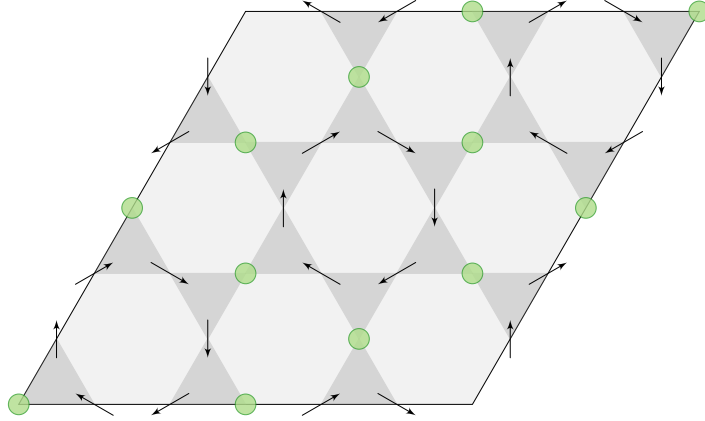
Figure 2.6: A diagram of the partially ordered phase present in Wills' ice, when second nearest-neighbour interactions are considered on the kagome lattice. When multiple states are averaged a partial order is present, where spins reside as shown by black arrows but the green dots are undecided. The green dots fail to order due to the hexagonal formation of the black arrows, none of which are second nearest-neighbours to the green sites. The exchange constants can be tuned to stabilize the green sites into an ordered state with green dots selecting identical Ising values. The corresponding to the ground state shown in Fig. 2.7 where the chosen Ising value of the disordered (green) spins defines a set of (blue) majority spins.

2.3 KAGOME ICE

Originally motivated by the rich nature produced from anisotropic $\langle 111 \rangle$ spins on the pyrochlore lattice, Wills *et al.* introduced a similar ferromagnetic model on the kagome lattice considering up to second nearest-neighbour interactions [50], with the Hamiltonian

$$H = -J_1 \sum_{\langle ij \rangle} S_i S_j - J_2 \sum_{\langle\langle ij \rangle\rangle} S_i S_j \tag{2.5}$$

Similar to the spin ice case the dot product of the nearest-neighbour Ising directions $\hat{S}_i \cdot \hat{S}_j = -1/2$, results in an effectively antiferromagnetic nearest-neighbour interaction. In a similar method to Pauling's estimate of the entropy for the proton disorder in water ice, the macroscopic degeneracy of this system can be estimated to be

$$S = \frac{Nk_B}{3} \ln\left(\frac{9}{2}\right) \tag{2.6}$$

Second nearest-neighbour perturbations added by Wills *et al.*, results in partial ordering shown in Fig. 2.6 for $J_2 < 0$ over a temperature range of $|J_2| S^2 < T < 1.5|J_2| S^2$. As J_2/J_1 is increased the partial ordering is removed, resulting in a long range order shown in Fig. 2.7. The stabilized state selects groups of majority spins arranged in a hexagonal fashion to tessellate the plane, for this reason we refer to this state as the *H-state*. The H-state was previously known as an exact solution to the ground state of the competing kagome Ising antiferromagnet with next nearest-neighbour interactions [51, 52].
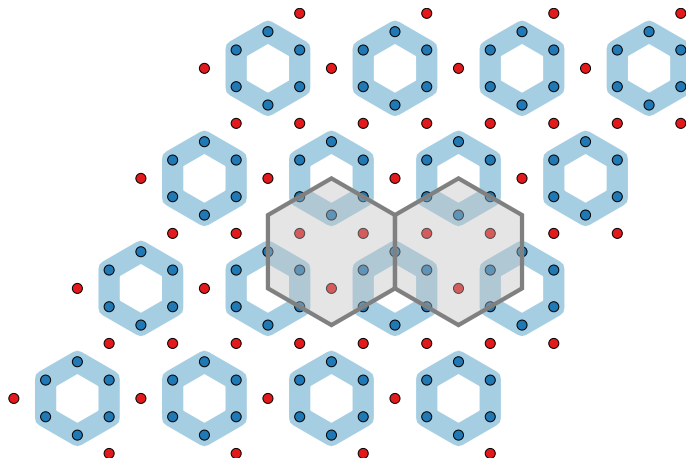
Figure 2.7: The H-state: ground state of Wills' ice and DKI with blue and red spins representing majority and minority spins respectively. Continuous chains of majority spins have been highlighted to emphasize the hexagonal ordering pattern. Two cells have been shaded in to indicate the 9-site magnetic unit cell.

2.3.1 *Dipolar Kagome Ice*

Work by Chern *et al.* extended the first and second nearest-neighbour model of Wills *et al.* to a long-range model through the inclusion of dipolar terms [53]. Chern *et al.* showed that the ground state for dipolar kagome ice (DKI) – the kagome lattice with *in-plane* moments interacting via a nearest-neighbour super-exchange and long-range dipolar term – is also the H-state [53]. Previous theoretical work had identified six-state clocks models such as DKI could order into such a state, in one of four ways [54]:

1. Two Kosterlitz-Thouless (KT) transitions

2. From the paramagnet state, the system undergoes an Ising transition followed by a transition of the 3-state Potts universality class

3. Same as (2) with the order of the Potts and Ising transitions reversed

4. A discontinuous phase transition between a paramagnet and an ordered phase.

Chern *et al.* provided numerical evidence that scenario (B) is at play: the system undergoes an Ising transition into a *charge ordered* state and then undergoes a transition of the 3-state Potts universality class into fully magnetically ordered state. We will review both of these transitions in detail beginning with charge ordering.

Charge ordering can be understood using the dumbbell model of DSI, first mentioned in Sec. 2.2.4 and applied to a triangle as shown in Fig. 2.8. Unlike the pyrochlore lattice where four sites are present per tetrahedron, the presence of three sites per triangle on the kagome lattice disallow a neutral charge configuration. We define the charge as

$$Q_\alpha = \pm \sum_{i \in \alpha} \sigma_i \tag{2.7}$$
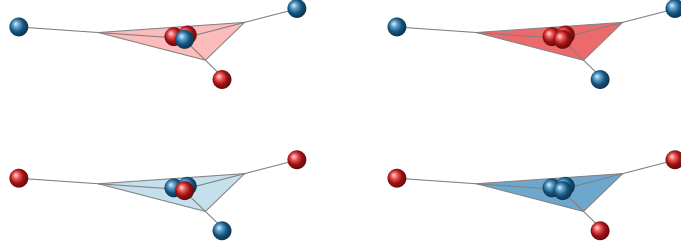
Figure 2.8: Charge on triangles, blue and red dots represent equal and opposite charges in the dumbbell convention of DKSI. The sum of these charges results in a non-zero strength of charge present for each triangle indicated by the colour of the triangle. This additional charge degree of freedom is resolved via various charge ordering patterns shown in Fig. 2.9.

where α is any triangle on the kagome lattice and σ_i is the Ising value of the moments located on the vertices of the triangles. The charge can be one of four possible values $Q_\alpha = \{\pm 3, \pm 1\}$ where $Q_\alpha = \pm 3$ corresponds to an all-in/all-out configurations and $Q_\alpha = \pm 1$ corresponds to a 2-in/1-out or 1-in/2-out. As the temperature is lowered, the system settles into an ice-like state reducing charges everywhere by removal of all $|Q_\alpha| = 3$ configurations. The remaining $|Q_\alpha| = 1$ charges order via an Ising transition into a *staggered* pattern on the lattice as shown in Fig. 2.9 (b) [53]. As the charges order into this staggered pattern, one third of the spins become a minority, obtaining equal Ising values. The minority spins decorate the kagome lattice such that no nearest-neighbour minority spin pairs exist. The remaining sites are filled by majority spins of opposite value satisfying the ice rules everywhere. The charge ordering is established through an Ising transition and reduces the Z_6 symmetry present in the Hamiltonian to a threefold symmetry. Thus from the four identified theoretical ordering scenarios, this suggests the next transition should be of the 3-state Potts universality class. Surprisingly, the Monte Carlo simulations performed by Chern *et al.*, provided no evidence of Potts' criticality on lattices up to $L = 36$ ($N = 3888$) [53]. Instead, a lack of singularity in the specific heat, suggested the magnetic transition may be of KT type – inconsistent with any of the four scenarios given above!

To better understand this unexpected result, Chern *et al.* mapped the system to dimer coverings on a honeycomb lattice with a second nearest-neighbour attractive interaction between dimers [53]. In the dimer mapping two possible defects exist:

1. triple-charge defects

2. charge-order defects

Triple-charge defects correspond to a violation of the ice-rules resulting in no dimers present on a site. Charge-order defects continue to respect the ice-rules but violate a *hardcore* dimer restraint on the honeycomb lattice, allowing for two dimers to be present on a given site. Due to the large energy difference between triple-charge and charge-
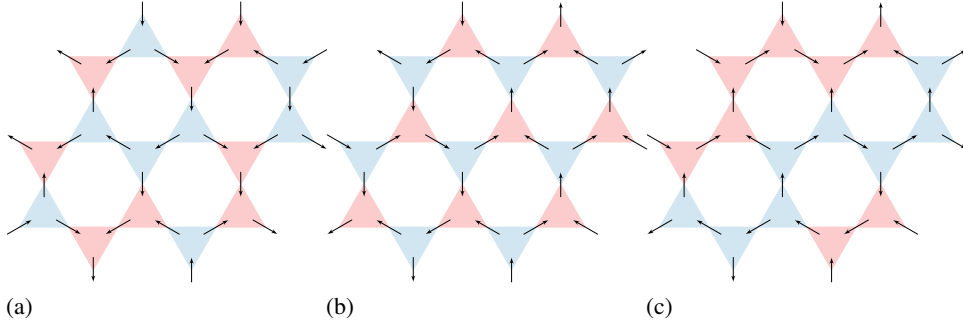
Figure 2.9: Three examples of charge ordering on dipolar kagome lattices: (a) random charge configuration (b) staggered charge order (c) striped charge order. Red and blue colours indicate charge imbalances resulting from the 2-in 1-out kagome ice rules shown in Fig. 2.8.

order defects, triple charge defects were ignored in their model. Charge-order defects were accounted for, by the addition of a fugacity term

$$z = \exp\left(-\frac{\epsilon}{k_B T}\right) \tag{2.8}$$

which recovers the hardcore-dimer limit as $\epsilon \to \infty$. Drastically different behaviour was observed, between models with $\epsilon \to \infty$ and $\epsilon < \infty$ [53]. For $\epsilon < \infty$, the correlation length is bounded by the charge defect dimer pairs, resulting in a magnetic ordering transition of the 3-state Potts universality class. The alternate case of $\epsilon \to \infty$ sets no such bound, allowing the average distance between charge defects to exceed the lattice size. When this occurs the system is once again in the hardcore limit and follows power-law spatial correlations, thus explaining the seemingly KT-like transition behaviour [53]. Thus the critical 3-state Potts behaviour is only then revealed for sufficiently large lattice sizes [55].

The work of Chern *et al.* highlights the non-trivial complications introduced from the addition of dipolar interactions. A natural extension of their work is to consider the effect of dipolar interactions on the kagome lattice with different spin orientations. Given that the H-state is the ground state for both the competing kagome Ising model and the DKI model, one might expect the ground state to be the same for the Ising antiferromagnet case where the moments are now taken *perpendicular* to the lattice.

2.3.2 *Dipolar Kagome Ising Antiferromagnet*

Given the large amount of effort invested in DKI Chioar *et al.* very recently considered the effects of adding dipolar interactions to antiferromagnetically coupled Ising spins on the kagome lattice [56]. In the dipolar kagome Ising antiferromagnet (DKA) model

21
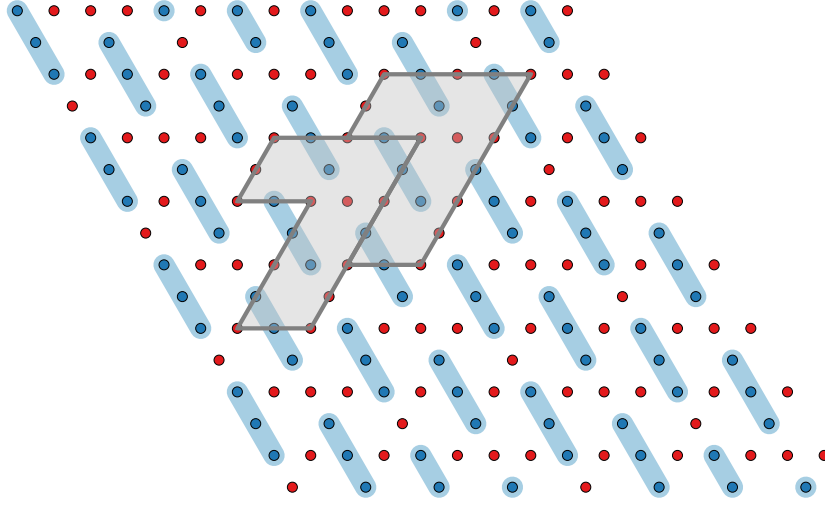
Figure 2.10: The 7-state: ground state candidate of DKA proposed by Chioar *et al.* [56], with red and blue spins representing majority and minority spins respectively. Continuous chains of majority spins have been highlighted to help demonstrate the 3-1-3-1-... pattern of majority minority spins. An additional continuous chain of minority spins have been highlighted to emphasize the continuous third neighbour chains of minority spins. Two cells have been shaded in to indicate the 12-site 7-shaped magnetic unit cell.

the local orientation of all spins is perpendicular to the plane allowing one to express the Hamiltonian in a more compact scalar form of

$$H = J \sum_{\langle \sigma_i \sigma_j \rangle} \sigma_i \sigma_j + D \sum_{i < j} \frac{\sigma_i \sigma_j}{r_{ij}^3} \tag{2.9}$$

where $r_{ij} = \left| r_i - r_j \right|$. Chioar *et al.* identified a candidate ground state, which we refer to as the 7-state, which had not been previously reported in the literature before, to the best the authors' knowledge [56]. It is characterized by a peculiar 12-site magnetic unit cell in the shape of a "7" as shown in Fig. 2.10, which tile the kagome plane in a rectangular fashion[2]. The 7-state is obtained via a two stage process similar to DKI scenario with a charge ordering transition followed by a magnetic ordering transition. However, the charge ordering of the 7-state results in a *striped*-charge ordered state, shown in Fig. 2.9 (c), as opposed to the staggered charge order of DKI [53, 56]. After the establishment of this *striped* charge order, the system, like most ice systems, suffers from an intrinsic slowdown of local dynamics. Interestingly however, the standard non-local technique typically used to remedy this[3], which has resolved all the other dipolar orderings addressed til now, also suffers an intrinsic slowdown [56]. To address this setback, Chioar *et al.* investigated the nature of domain walls in the 7-state to propose a new clustering method. The method proposes to decompose the low temperature states into series of trapezoids, each with 9 possible *spin swaps* shown in Fig. 2.11. Of the

---

2 It should be noted an equivalent rhomboidal unit cell choice could have been chosen

3 which will be discussed in the following chapter

(a)   (b)
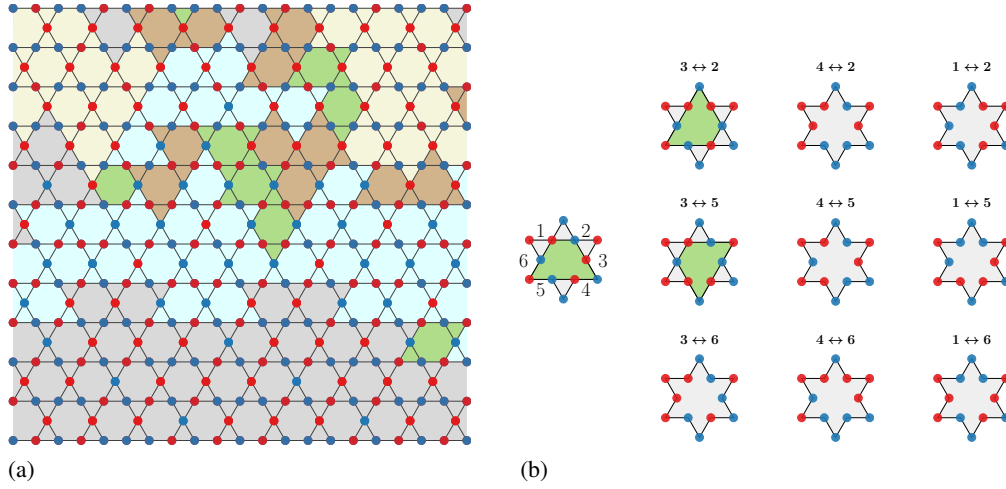
Figure 2.11: Figure reproduced from Ref. [56]: Observed domain walls of the 7-state formed by tessellated pentagonal configurations of spins are shown in (a). Relations between pentagonal configurations can be generated by swapping spins on the inner hexagonal ring of a 9-site unit cell as shown in (b). Of these nine swaps, three result in rotated orientations of pentagonal configurations indicating the potential of a clustering algorithm which promotes a preferential selection of these configurations.

nine spin swaps only two preserve the initial trapezoidal configuration through rotation, suggesting a possible subset of favourable local configurations [56]. If these spin swaps can then be carefully selected, they may provide a technique to efficiently search the DKA energy manifold.

2.4 CHAPTER SUMMARY

In this chapter, we presented a wide variety of ordering patterns for dipoles on various lattices and the effects of geometric coupling with various high symmetry fields was discussed. Exploitations of the various couplings for in-field systems have been discussed, which allow for a better understanding of the DSI Hamiltonian. The fractionalization of dipolar excitations and emergence of magnetic monopoles was introduced by discussing the concept of the dumbbell picture and charge. We have discussed the special case of DSI in a moderate [111] field – DKSI – where an intermediate plateau in the magnetization results from macroscopically degenerate states in the kagome planes, governed by a set of kagome ice rules. In an attempt to gain some intuition on the potential ground state of DKSI, a review of dipole ordering on two dimensional kagome lattices was provided. While each two dimensional system exhibits a complex two part ordering transition, the differences between their spin angles is sufficient to introduce unique ground states to each. Each of these systems will be revisited in later chapters in relation to the ground state of DKSI.

3

METHODS

3.1 MONTE CARLO SIMULATIONS

3.1.1 *Monte Carlo Methods*

Numerical methods far predate machines with famous techniques for finding roots, interpolating polynomials and approximating irrationals [57]. Of these numerical techniques, the particular method of *statistical sampling* has seen great success in modern times and has been developed to solve highly complicated statistical physics problems. The literature today often refers to statistical sampling as *Monte Carlo Methods*, a term coined by Nicholas Metropolis in 1949, referring to the famous casino in Spain [58].

Originally, the Monte Carlo Method was developed in the context of how many ways a deck can be shuffled such that if it is used for a game of Solitaire, the game has a possible solution [59]. While the rules which govern the game solitaire are relatively simple, the sheer amount of ways a deck can be shuffled – 52! – is so large a combinatorial approach would prove to be very difficult. Instead of exhausting all possibilities using brute force, Monte Carlo methods reduce the problem to sampling a set of possibilities drawn from a probability distribution [59].

3.1.2 *The Metropolis-Hastings Algorithm*

One extremely popular method for sampling from a probability distribution in statistical physics is the Metropolis-Hastings algorithm, which we will review closely following Newman and Barkema's exposition [58]. Consider a system where every state can be defined through a transition probability $P(\nu|\mu)$ between the current state of the system μ and a new state ν. The Metropolis Hastings algorithm is used to produce a set of states from the *stationary distribution* $\pi(\mu)$ which converges to the *desired probability distribution* $P(\mu)$. A solution exists given a unique stationary distribution $\pi(\mu)$ exists, ensured by two conditions [60]:

- **Detailed Balance**: Each transition from $\mu \to \nu$ is reversible for all pairs of μ and ν. That is, for every pair μ and ν, the probability of being in ν and transitioning to μ is equal to the probability of being in ν and transitioning to μ.

- **Ergodicity**: The system does not return to any state at a fixed number of transitions and the expected number of transitions at which a system returns to a state is finite.

We begin by setting our stationary distribution $\pi(\mu)$ equal to the desired distribution $P(\mu)$. This equality can be guaranteed given equilibration conditions defined later, for now, we ensure condition (1) is met by starting with Baye's theorem [60].

$$\pi(\mu)P(\nu|\mu) = \pi(\nu)P(\mu|\nu)$$
$$P(\mu)P(\nu|\mu) = P(\nu)P(\mu|\nu)$$
$$\frac{P(\nu|\mu)}{P(\mu|\nu)} = \frac{P(\nu)}{P(\mu)} \tag{3.1}$$

We set $P(\nu|\mu) = g(\nu|\mu)A(\nu|\mu)$ splitting the probability distribution $P(\nu|\mu)$ into a *joint distribution* comprised of a *proposal* distribution $g(\nu|\mu)$ and an *acceptance* distribution $A(\nu|\mu)$. Rearranging and solving for the acceptance distribution we obtain

$$\frac{A(\nu|\mu)}{A(\mu|\nu)} = \frac{P(\nu)}{P(\mu)} \frac{g(\mu|\nu)}{g(\nu|\mu)} \tag{3.2}$$

One solution satisfying the above condition is the Metropolis criterion where

$$A(\nu|\mu) = \min\left(1, \frac{P(\nu)}{P(\mu)} \frac{g(\mu|\nu)}{g(\nu|\mu)}\right) \tag{3.3}$$

To simulate relevant thermodynamic quantities of interest, our desired probability distribution is given by the partition function

$$Z = \sum_\omega \exp\left(-\beta E_\omega\right) \tag{3.4}$$

where the sum runs over all microstates ω, with the corresponding energy E_ω and $\beta = 1/(k_B T)$, where k_B is the Boltzmann constant and T is the temperature of the system. Since the sum of all probabilities must be equivalent to 1, the probability of finding the system in any given state μ is

$$P(\mu) = \frac{1}{Z} \exp\left(-\beta E_\mu\right) \tag{3.5}$$

Thus the Metropolis criterion becomes

$$A(\mu|\nu) = \min\left(1, \exp\left(-\beta\Delta E\right) \frac{g(\mu|\nu)}{g(\nu|\mu)}\right) \tag{3.6}$$

The only remaining unknown term, $g(\mu|\nu)$, left in the Metropolis criterion can be addressed by implementing a symmetric proposal distribution whereby $g(\mu|\nu) = g(\nu|\mu)$ such as a random walk [60]. After a transient time period when the system has reached a *thermal equilibrium* to ensure $\pi(\mu) = P(\mu)$, the Metropolis criterion fully satisfies the required conditions and one may draw from the distribution to simulate thermodynamic quantities of interest. From the partition function, *estimators* can be constructed to approximate true physical thermodynamic quantities for a system of N spins, such as the specific heat

$$C = \frac{1}{Nk_B} \frac{\langle E^2 \rangle - \langle E \rangle^2}{T^2} \tag{3.7}$$
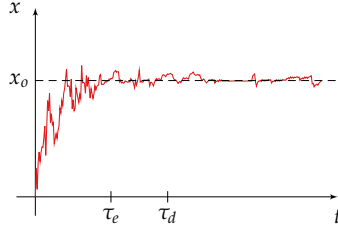
Figure 3.1: An illustration of estimator behaviour over time: as time progresses the estimator x converges to a value of x_o representative of its true physical value. The minimal time required for the estimator to fluctuate about a mean value of x_o is τ_e known as the auto-correlation time. In practice, a cutoff time of τ_d greater than τ_e is often used to more simply account for the equilibration time required before sampling.

Up to this point, it has been taken for granted that $\pi(x) = P(x)$, which is only valid when equilibration is met. Therefore, before constructing an implementation of the Metropolis Hastings algorithm we will need to define what is meant by equilibration.

3.1.2.1 *Equilibration*

As discussed in Sec. 3.1.2, a necessary condition for the validity of our simulations is that the system is evolved over sufficient time to equilibrate. Strictly, one can define a quantity called the *autocorrelation time* measuring the randomness from which one draws samples from a given distribution. This autocorrelation time is characterized by a time τ_e where a sufficient number of transitions have occurred that the system is sufficiently different from where it started [58]. Many techniques to rigorously calculate τ_e, descriptions of which can be found in Ref. [58] but one can also infer visually some discard time τ_d sufficiently higher than τ_e to avoid such strict monitoring of the system. Visually, this corresponds to when the estimator converges to a mean within statistical error of estimators from other multiple independent simulations, this convergence is shown in Fig. 3.1. In both cases, the amount of time required to reach thermal equilibrium is measured in *Monte Carlo sweeps* (MCS) where a sweep constitutes N trials (proposed transitions), where N is the number of sites present in the system. In this work we employ a τ_d equal to 10% of the total amount of MCS used in simulation.

Thus an implementation of the Metropolis Hastings algorithm can be constructed as follows:

1. Begin with a microstate μ

2. Perturb μ to obtain a new microstate ν

3. Calculate $\Delta E = E_\nu - E_\mu$

   3.1. If $\Delta E \leq 0$ go to (4)

   3.2. Generate a random number x, from a uniform distribution between 0 and 1

   3.3. If $x \leq \exp(-\beta \Delta E)$: go to (4), else go to (2)

4. Update the system such that $\mu \to \nu$

5. If MCS $> \tau_e$: proceed, else go to (2)

6. Calculate estimators

7. If MCS $>$ MCS$_{\text{total}}$: break, else go to (2)

Where MCS is the current number of sweeps performed and MCS$_{\text{total}}$ is the total number of sweeps to be performed for a simulation.

Since τ_e of a simulation is measured by the amount of MCS, efficient procedures to reduce the number of MCS is crucial in developing feasible Monte Carlo simulations. These procedures can be grouped into two sets which account for sampling the macrostates and microstates of the system. We will address the issue of sampling from macrostates first.

3.1.2.2 *Simulated Annealing & Parallel Tempering*

Given a sufficiently large amount of total Monte Carlo sweeps (MCS), theoretically, any estimator must converge to its true physical result. However, this is somewhat of a hollow promise as the time scales required may still be computationally infeasible. To combat this, a technique called *simulated annealing* can be used in optimization problems such as identifying the free-energy global minimum from many other local minima [61]. Simulated annealing is a technique in which a system is systematically cooled in a manner such that equilibration is met at every temperature point. At high temperature, the system retains a large amount of thermal disorder, allowing it to effectively sample the state space. As the system cools, it settles into increasingly ordered states better minimizing the energy, until finally at $T = 0$ a minimal energy configuration is obtained. Depending on the complexity of the state space, one must ensure that the system is cooled sufficiently slowly to allow adequate exploration of the free-energy landscape. Without an adequate search of the macroscopic state, only a local optimum would be achieved finding a *metastable* state. An illustration of this process is provided in Fig. 3.2.

Other more sophisticated techniques in helping identify the global minimum of the free-energy exist, such as *parallel tempering* [61]. In parallel tempering a fixed amount of simulations are threaded to run at different temperatures concurrently. Upon a set number of moves, a swap of system configurations for simulations with adjacent temperature points is proposed. The proposed swap is again accepted using the same Metropolis criterion as before, namely the swap is accepted with probability

$$A\left(\nu|\mu\right) = \min\left(1, \exp\left(\left(E_\nu - E_\mu\right)\left(\frac{1}{k_B T_\nu} - \frac{1}{k_B T_\mu}\right)\right)\right) \quad (3.8)$$

Provided temperature points are spaced optimally, parallel tempering can provide an excellent way of sampling the state space [61].
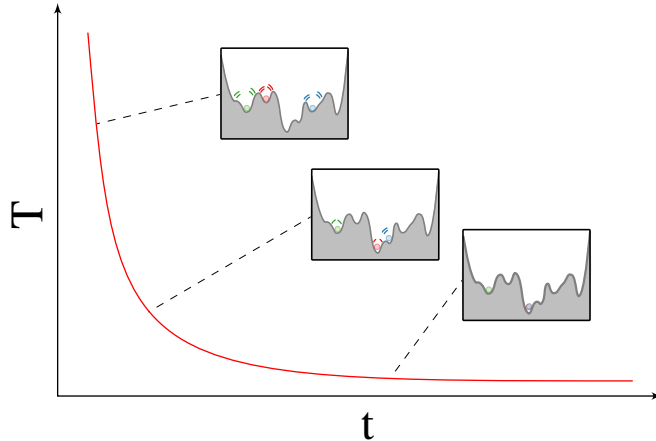
Figure 3.2: An illustrative explanation of simulated annealing, where multiple simulations undergo a cooling process indicated by the red curve. At high temperature, the state of systems (red/blue/green dots) cover a large portion of the state space, due to thermal disorder represented by radiating lines around dots. As the systems cools states and thermal disorder is reduced, local minimal energy states are found which approximately minimize the free-energy landscape indicated by gray regions. If the cooling protocol is too rapid, these local minimal free-energy states do not correspond to the global minimal states as indicated by the trapped green dot which failed to find the global minimum. A potential well beneficial enough to trap system from easily fluctuating out is referred to as a metastable state.

Finally both parallel tempering and simulated annealing can be further improved through *trivial* parallelization. In trivial parallelization, estimators from multiple independent simulations are averaged to provide a more complete description of the state space. While the least sophisticated of the equilibration techniques, trivial parallelization will play an important role in the addressing the complicated dynamics of DKSI.

3.1.2.3 *Loop Moves*

While techniques such as simulated annealing and parallel tempering provide methods of improving sampling between macrostates, the subject of sampling between microstates still remains. For most Monte Carlo simulations where the energy manifold is sufficiently smooth the use of a *single spin flip* update is adequate for transitioning between microstates. Such local alterations used to move between microstates are defined as *local* dynamical processes.

In DSI the sampling problem is more extreme where local dynamical processes which usually work in other systems violate the ice-rule manifold which ensure a set of 2-in 2-out ice rules. Single spin flip violations of these rules cost an energy of $\Delta E = 4J_{\text{eff}}$, resulting in the acceptance rate dropping exponentially as $\exp(-4J_{\text{eff}}/k_B T)$ [38]. However, as mentioned in Sec. 1.3, the ice-rule manifold for DSI is quasi-degenerate and a set of long-range dipolar interactions remain to be minimized. Such a strong penalty for local updates and the extensiveness of the ice manifold, make it infeasible
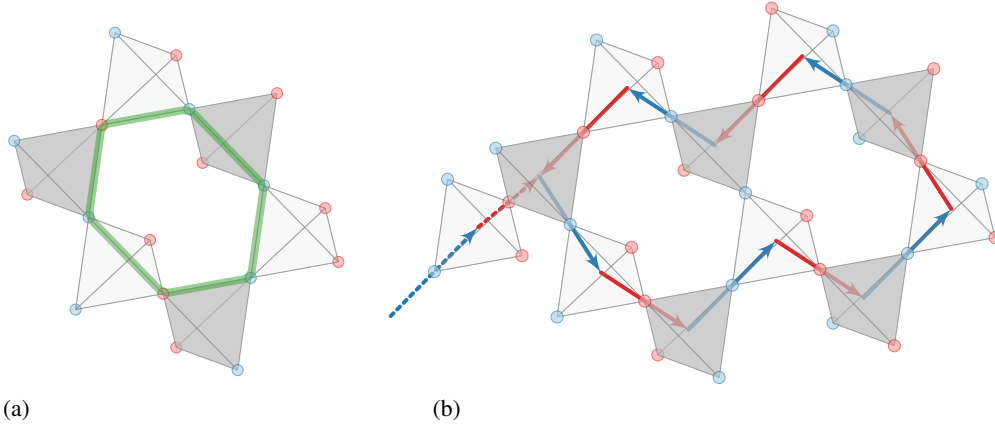
Figure 3.3: Portions of the pyrochlore lattice demonstrating (a) quasi-zero modes and (b) generalized loop moves. Red and blue dots represent inward and outward pointing Ising moments while red and blue arrows indicate a sequence of spins randomly chosen in a head to tail sequence. Green highlighting indicates a non ergodic selection of the minimal loop configuration which tunnels between ice states. The ergodic loop move indicates an ergodic selection of loops signified by a random path traced out until self-intersection decomposing the path in to a tail and loop indicated by dashed and solid lines respectively.

to expect the SSF to robustly predict the true ground state of DSI. Thus a non-local method to tunnel between ice-states to resolve dipolar correlations is required.

To construct a non-local sampling method, we seek to perform a finite number of single spin flip moves simultaneously. The smallest possible sequence of moves which can tunnel between the ice states, is given by a 6 site hexagonal plaquette with alternating inward and outwardly pointing spins as shown in Fig. 3.3(a). Such *plaquette* moves were first identified by Anderson[1]. However, while these plaquette moves respect detailed balance, they do not obey ergodicity, due to an inability to introduce a finite change in the magnetization of the material. Therefore any two ice-states with different magnetizations such as the $q = 0$ and $q = X$ states shown in Fig. 2.2 cannot be connected within a finite number of plaquette moves. To create a move which respects ergodicity, the plaquette move can be extended to a more general *loop* move, where loops are arbitrarily long. With no such restriction of lengths, *spanning* loops which traverse the periodic boundary conditions (PBCs) and can introduce a finite change in magnetization allowing the connection of separate magnetic spin ice sectors. Thus loop moves are ergodic and allow for a full sampling of the spin ice states.

With ergodicity being obeyed, we seek an algorithm which constructs loops while obeying detailed balance. We propose the following algorithm generalized from the outline of Newmann and Barkema [58] and implemented in spin ice by Melko *et al.* [13]:

1. select a random site σ_i and set $i = 0$

---

1 In the context of Anderson's paper [6] the plaquette moves were noted as short range ordered structures and *not* as a possible statistical sampling method.

2. randomly select a nearest-neighbour spin σ_{i+1} such that $\sigma_{i+1} = -\sigma_i$ from a tetra-hedron where the moment of σ_i is defined as inward

3. add σ_{i+1} to a list of spins and set $\sigma_i \rightarrow \sigma_{i+1}$

4. terminate if:

    a) a nearest-neighbour of σ_{i+m} which we denote as σ_{i+l} exists within the list populated by (2)

    b) no $\sigma_{i+1} = -\sigma_i$ candidates exist

5. go to (2)

When condition (4.a) is met, one can deconstruct the populated list into a loop $L = \{\sigma_l, \sigma_{l+1}, ..., \sigma_m\}$ and a left over tail $T = \{\sigma_0, \sigma_1, ..., \sigma_l\}$. An illustration of this algorithm and the resulting sets is provided in Fig. 3.3. We define a long loop when no tail exists and a short loop when a tail exists

Detailed balance can be straightforwardly shown by considering the probability of constructing each set. The probability of selecting a given starting site, specifically σ_0, in a system of N particles is $1/N$. In the ice rule manifold, each tetrahedron has two spins of opposite sign to select from giving the probability of construct T as 2^{-l}. Similarly, the probability of constructing L is $2^{-(m-l)}$, thus the probability of transitioning between states is

$$g(\nu|\mu) = \frac{1}{N}2^{-l}2^{-(m-l)} = \frac{2^{-m}}{N} \tag{3.9}$$

Upon reversal of L, T is left unaffected giving a probability again of 2^{-l} and $1/N$ for selecting σ_0. While the original connection of σ_{l-1} to σ_l is now impossible, the reverse direction σ_{l-1} to σ_m is now possible giving a probability again of $2^{-(m-l)}$. Combining these probabilities we obtain

$$g(\mu|\nu) = \frac{1}{N}2^{-l}2^{-(m-l)} = \frac{2^{-m}}{N} \tag{3.10}$$

which is identical as before, therefore proving the loop move respects detailed balance.

Thus satisfying both ergodicity and detailed balance, the loop move provides a non-local Monte Carlo move for sampling between various ice states. The now widespread use of the loop move in the spin ice community is a testament to the effectiveness of such a Monte Carlo move. The first implementation of this loop move in spin ice was by Melko *et al.* who showed it to resolve low temperature dipolar correlations in ice materials, identifying the [001] ground state in zero field DSI, as discussed in 2.1 [13]. While an excellent sampling technique for zero field systems, some simple probabilistic arguments will show potential improvements of the loop move for in-field systems.

3.1.3 *Kagome Loop Moves*

Consider the loop move applied to a system subject to a [110] magnetic field, where the field decomposes the pyrochlore lattice into two subsets of perpendicular and in-line spins, as discussed in Sec. 2.2.3 and illustrated in Fig. 2.2 (b). The [110] field

couples with the α-chains, while the β-chains, which are perpendicular to the field, remain uncoupled. Consider a scenario where the magnetic field has been increased sufficiently to pin the α-spins. As $T \to 0$ it is easy to see that the dynamics of the system is set by the thermally active β-chains, and calculate the probability of constructing these β-chains using the loop move presented thus far. Given half the sites are β-chains, the probability of selecting a β-chain spin for σ_0 is 2^{-1}. Each subsequent step of the construction has a 2^{-1} chance of landing on an α or β spin. Thus, the probability of constructing L then is $2^{-\ell}$ where ℓ is the length of the loop which grows as the size system. Thus the probability of constructing a β-chain decreases exponentially with increasing system size. This enormous inefficiency in the loop construction can be easily remedied by excluding all α-chain spins during the construction process.

A similar problem arises in DKSI when the applied field is along the [111] direction. As shown in Fig. 2.3, application of the [111] field decomposes the pyrochlore lattice into alternatingly stacked triangular and kagome layers. In DKSI, the sites residing on the triangular lattice are pinned. Thus any loop containing triangular site spins is less thermally active then any loop composed solely of spins from kagome sites. Thus in the DKSI regime, we require a non-local move which samples the fluctuations occurring in the kagome plane.

We introduce the *kagome loop move*, a loop move which during construction ignores nearest-neighbour spins residing on the triangular lattices of the pyrochlore lattice. Given this loop move is a subset of the all possible loop moves, it inherits the property of detailed balanced and is able to sample the topological sectors of DKSI [63]. We will revisit the effectiveness of the kagome loop moves in Sec. 4.2.3, after the results of simulations have been presented.

3.2 EWALD SUMMATION

An important aspect of this work is the correct handling of the long range dipolar interactions, a proper implementation of which is notoriously tricky to handle for two reasons:

1. an explicit sum of the dipolar interactions is slow and conditionally convergent

2. every spin interacts with all other spins in the system, making the calculation of dipolar energies expensive

The first problem can be solved using the well-known *Ewald Method* [16] which splits the explicit sum Eq. 3.11 into direct and reciprocal space sums. Both sums are absolutely and rapidly convergent, allowing one to effectively account for all interactions within the finite system and between periodic replicas.

In this section, we briefly outline a physically motivated derivation of the Ewald Method for an arbitrary unit cell and translation vector. The derivation presented follows that of Allen [64], written in a similar notation as Wang and Holm [65]. A more mathematically oriented approach can be found in references [66, 67].

We begin by explicitly writing the dipole-dipole Hamiltonian for a system of N dipoles with moments $\boldsymbol{\mu}_i$ located within a unit cell at position $\boldsymbol{r}_i$. Upon application of PBCs, the Hamiltonian becomes

$$H = \frac{1}{2} \sum_{i=1}^{N} \sum_{j=1}^{N} \sum_{\boldsymbol{n}}{}' \left(\frac{\boldsymbol{\mu}_i \cdot \boldsymbol{\mu}_j}{\left| \boldsymbol{r}_{ij} + \boldsymbol{n} \right|^3} - 3 \frac{\boldsymbol{\mu}_i \cdot \left(\boldsymbol{r}_{ij} + \boldsymbol{n} \right) \boldsymbol{\mu}_j \cdot \left(\boldsymbol{r}_{ij} + \boldsymbol{n} \right)}{\left| \boldsymbol{r}_{ij} + \boldsymbol{n} \right|^5} \right) \tag{3.11}$$

where $\boldsymbol{r}_{ij} = \boldsymbol{r}_j - \boldsymbol{r}_i$, the prime denotes the omission of $i = j$ pairs for $\boldsymbol{n} = 0$, where $\boldsymbol{n}$ is a set of replica copies given by

$$\boldsymbol{n}^{(\gamma)} = \sum_{m \in \mathbb{Z}} \left(m \cdot \left(A_1^{(\gamma)} + A_2^{(\gamma)} + A_3^{(\gamma)} \right) \right) \tag{3.12}$$

where γ is a component of $\boldsymbol{n}$ and A_i are the translational vectors of the unit cell. The sum over $\boldsymbol{n}$ is performed in a spherical manner outwards. For example the first two parts of a sum performed on a cubic lattice of length L is $(0, 0, 0)$ and then $(\pm L, 0, 0)$, $(0, \pm L, 0)$, $(0, 0, \pm L)$. The effect of the spherical boundary defined by the sum of periodic replicas is determined by

$$U^{(\text{surf})} = \frac{2\pi}{(2\epsilon_s + 1) V} \sum_{i=1}^{N} \sum_{j=1}^{N} \boldsymbol{\mu}_i \cdot \boldsymbol{\mu}_j \tag{3.13}$$

where the value of the relative permittivity ϵ_s determines the behaviour of the surrounding medium. A value of $\epsilon_s = 1$ corresponds to a vacuum while a value of $\epsilon_s' = \infty$ accounts for the system surrounded by an excellent conductor. Calculations where $\epsilon_s = 1$ have a non-vanishing term due to a build up of charge on the layer of the spherical surface [14, 28]. Calculations using $\epsilon_s = \infty$ also known as metallic or reflective boundary conditions are embedded in a conductor and have no such layer. Experimentally, this embedding in a conductor, corresponds to a needle like bulk sample, parallel to an applied field, with no internal demagnetizing field [14, 28]. Since this work is concerned with the simplest case of DKSI, we take a metallic boundary condition negating this surface term.

Each dipole on the lattice is given an associated charge distribution of equal magnitude and opposite sign, in the form of a Gaussian [2],

$$\rho_i^{\mu}(\boldsymbol{r}) = \mu_i \alpha^3 \exp \left(-\frac{\alpha^2 r^2}{\pi^{3/2}} \right) \tag{3.14}$$

where α and $\boldsymbol{r}$ determine the width and $\boldsymbol{r}$ radial position relative to the center of the Gaussian distribution. The purpose of these artificial charges is to effectively *screen* the charges – essentially shielding the interactions of the spins from the system. By suppressing the dipolar interactions the long-range nature is reduced to short range interactions described in real space by $H^{(r)}$. Since artificial constructs were added to the

---

2 The choice of a Gaussian is convenient but not necessary as demonstrated by Berthaut and Heyes who use 9 other possible distributions [67, 68]

system to obtain this result, a second cancelling charge distribution $H^{(k)}$ is then added *in reciprocal space* to remove excess charge from the system. Finally, the special $k = 0$ case of the reciprocal sum requires special attention to remove an energetic self contribution $H^{(self)}$ present in the cancelling distribution centered at r_i with itself. Thus the final Hamiltonian is broken into three parts

$$H = H^{(r)} + H^{(k)} - H^{(self)} \tag{3.15}$$

with the respective parts given by

$$
H^{(r)} = \frac{1}{2} \sum_{i=1}^{N} \sum_{j=1}^{N} \sideset{}{'}\sum_{n} \left[\left(\boldsymbol{\mu}_i \cdot \boldsymbol{\mu}_j \right) B \left(\left| r_{ij} + n \right| \right) \right.
$$
$$
\left. - \left(\boldsymbol{\mu}_i \cdot \left(r_{ij} + n \right) \right) \left(\boldsymbol{\mu}_j \cdot \left(r_{ij} + n \right) \right) C \left(\left| r_{ij} + n \right| \right) \right] \tag{3.16}
$$

$$
H^{(k)} = \frac{1}{2V} \sum_{k \neq 0} \frac{4\pi}{|k|^2} \exp \left(\frac{|k|^2}{4\alpha^2} \right) \sum_{i=1}^{N} \sum_{j=1}^{N} \left(\boldsymbol{\mu}_i \cdot k \right) \left(\boldsymbol{\mu}_j \cdot k \right) \exp \left(\cos \left(k \cdot r_{ij} \right) \right) \tag{3.17}
$$

$$
H^{(self)} = \frac{2\alpha^3}{3\sqrt{\pi}} \sum_{i=1}^{N} |\boldsymbol{\mu}_i|^2 \tag{3.18}
$$

where, V is the volume of the unit cell and

$$
B(r) = \frac{1}{r^3} \left[\mathrm{erfc}\,(\alpha r) + \left(\frac{2\alpha r}{\sqrt{\pi}} \exp \left(-\alpha^2 r^2 \right) \right) \right] \tag{3.19}
$$

$$
C(r) = \frac{1}{r^5} \left[3\mathrm{erfc}\,(\alpha r) + \left(\frac{2\alpha r}{\sqrt{\pi}} \exp \left(-\alpha^2 r^2 \right) \right) \left(3 + 2\alpha^2 r^2 \right) \right] \tag{3.20}
$$

where, similar to n, k is a set of replica copies in reciprocal space summed spherically outwards given by

$$
k^{(\gamma)} = \sum_{m \in \mathbb{Z}} \left(m \cdot \left(B_1^{(\gamma)} + B_2^{(\gamma)} + B_3^{(\gamma)} \right) \right) \tag{3.21}
$$

where, B_i are reciprocal lattice vectors. The value α is often referred to as the *splitting parameter*, as it determines how the direct sum is "split" between the real and reciprocal space sums – essentially it dictates how far the spherical summations must be performed to attain convergence [65]. While calculations exist for optimal splitting parameter, often, in practice, the case $\alpha = 1$ is taken to allow the computer to reduce the number of operations performed.
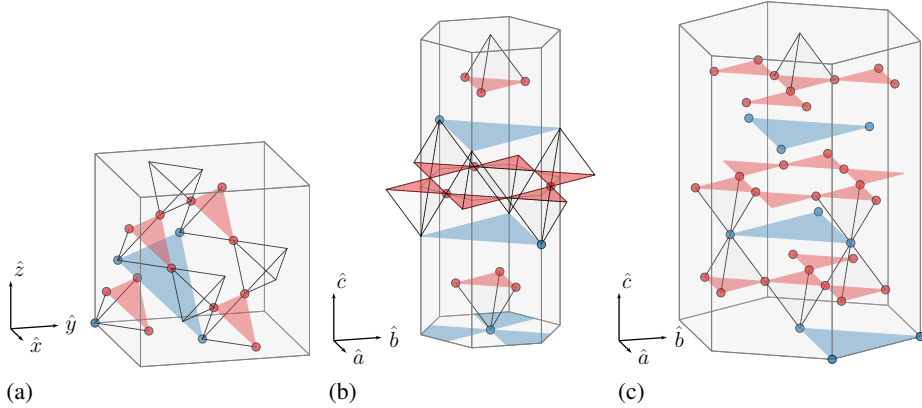
Figure 3.4: Cubic (a) and hexagonal (b)/(c) unit cells of the pyrochlore lattice shown with corresponding cubic and hexagonal coordinate systems in the lower let corners. Triangular and kagome planes have been highlighted in blue and red, respectively, to help illustrate the quasi-2D structure of interleaving structures which occur in the pyrochlore lattice motivated in Fig. 2.3. The coordinates of these unit cells are tabulated in Appendix. A along with the moments of spins in cubic and hexagonal bases.

The Ewald energy E_{ij} for a pair of dipoles μ_i and μ_j can be stored in a matrix and the corresponding dipolar interaction for an Ising system calculated at any time by

$$
H_{\text{dipole}} = \begin{pmatrix} \sigma_1 \\ \sigma_2 \\ \vdots \\ \sigma_N \end{pmatrix}^T \begin{pmatrix} 0 & E_{12} & \dots & E_{1N} \\ E_{21} & 0 & \dots & E_{2N} \\ \vdots & \vdots & \ddots & \vdots \\ E_{N1} & E_{N2} & \dots & 0 \end{pmatrix} \begin{pmatrix} \sigma_1 \\ \sigma_2 \\ \vdots \\ \sigma_N \end{pmatrix} \tag{3.22}
$$

However, storage of this Ewald matrix grows as $\mathcal{O}\left(N^2\right)$ requiring an enormous amount of memory on a computer! If one wishes to use the Ewald matrix an alternative implementation to the naive matrix multiplication is required. A solution has been provided in Appendix. B for the benefit of the reader who might be interested in implenting his/her own Ewald subroutine.

3.2.1 *Choice of Unit Cell*

With the general formulae (3.16, 3.17 and 3.18) for the Ewald Method defined, a choice of unit cell remains to be made. Usually, in Monte Carlo simulations of spin ice, the *conventional* cubic unit cell comprised of 16-sites as shown in Fig. 3.4 (a) is taken. The cubic unit cell provides an easily implementable set of translational vectors and basis often commensurate with magnetically ordered states, for example, the [001] and $q = X$ state. However, given the quasi-2D nature of DKSI and the complicated physics present in DKI and DKA; one might expect that the cubic unit cell is not the most "natural" implementation of the pyrochlore lattice for simulating DKSI.

(a)   (b)
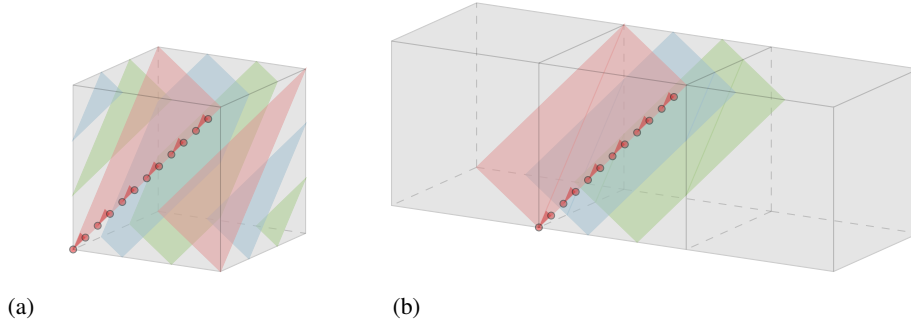
Figure 3.5: A $[3,3]_{\mathrm{cube}}$ system is illustrated in (a) with the 3 unique kagome planes highlighted by considering all spins in the system which are connectible by nearest-neighbours while excluding spins residing on triangular layers. The PBC unwrapped version is given in (b) to demonstrate how these kagome planes are connected when considering multiple copies subjected to the PBCs. Spins residing on the red slice of kagome lanes which also exist on the face of the non-replica unit cell have been drawn in both (a) and (b) for reference.

Consider a candidate ground state for DKSI where each kagome plane supports an H-state configuration and the inter-plane correlations are minimized through some stacking pattern. For the H-state to be commensurate with the kagome planes formed by cubic unit cells, the magnetic unit cell of the H-state must appropriately wrap around the cubic periodic boundary conditions (PBC) as shown in Fig. 3.5. By inspection for an $L \times L \times L$ cube, an equivalent network of tetrahedra using translational cubic unit vectors can be expressed as L layers of $2L \times 2L$ tetrahedra arranged to form stacked kagome planes. Therefore the H-state is only commensurate with systems formed of cubic unit cells when the side length is a multiple of three, resulting in system sizes growing in multiples of 432 spins!

An alternative to the cubic unit cell can be constructed by creating a 3D analogue of the H-state magnetic unit cell. Recall the pyrochlore lattice can be decomposed into an alternating series of triangular and kagome planes stacked in an ABC fashion as shown in Fig. 2.3. Given this, one can stack multiple H-state magnetic unit cells in an ABC fashion, filling in the required triangular sites between to construct a unit cell of the pyrochlore lattice as shown in Fig. 3.4 (c). In this way, any system formed by these 36-site hexagonal unit cells will have kagome planes which are always commensurate with the H-state.

After constructing the 36-site unit cell, one can ask if any other hexagonal unit cells exist with a different number of spins present in the system. By inspection of the 2D kagome lattice, one can see that there is also a 12-site and 144-site hexagonal prism unit cells constructable. The 12-site hexagonal prism unit cell as shown in Fig. 3.4 (b) allows a finer sampling of possible systems sizes. The 144-site hexagonal prism unit cell can be seen to be equivalent to a $2L \times 2L$ 36-site hexagonal unit cell and thus provides no additional benefits of accessing different system sizes. To fully explore as many systems sizes as possible, we use a combination of the conventional cubic unit cell and both the
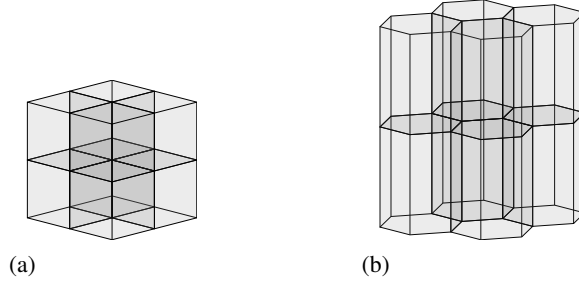
Figure 3.6: Examples of $L \times L \times H$ cubic and hexagonal unit cell configurations given by the $[L, H]$ convention used hereafter in this work. The notation for (a) and (b) are respectively $[2, 2]_{\text{cube}}$ and $[2, 2]_{\text{hex}}$, for the latter case an additional superscript denotes the sites present within the unit cell.

36- and 12-site hexagonal unit cells. The use of these many various unit cells, aim to accommodate as many potentially different long-range ordered magnetic unit cells as possible.

With three unit cells now present, it is useful to formulate a compact notation which easily identifies systems constructed from them. For the rest of this work, an $L \times L \times H$ system formed by cubic unit cells will be denoted as $[L, H]_{\text{cube}}$. Similarly, an $L \times L \times H$ system formed by hexagonal unit cells will be denoted as $[L, H]_{\text{hex}}$, with an additional superscript denoting the number of sites present in the cell. For example a $4 \times 4 \times 2$ arrangement of 12-site hexagonal unit cells is referred to as $[4, 2]_{\text{hex}}^{12}$, while a $4 \times 4 \times 2$ arrangement of 36-site hexagonal unit cells is referred to as $[4, 2]_{\text{hex}}^{36}$ An example showing $[4, 2]_{\text{hex}}$ and $[2, 2]_{\text{cube}}$ configurations is given in Fig. 3.6 . The long range magnetic order

3.3 MEAN FIELD THEORY

In physics, a great amount of knowledge can often be gained by approximating complex systems into simplified and readily interpretable systems. While these simplified models fail to grasp the gory details of a problem they are often successful in encapsulating some of the essential components of the complex models. In statistical physics, a common simplified model which is broadly applicable to problems is *mean field theory* (MFT). Our derivation of the MFT equations for this problem follows that of Parisi [69]. Consider a system where the probability distribution can be factorized into the general form

$$P[\sigma] = \prod_i P_i(S_i) = \prod_i \left(\left(\frac{1 + m_i}{2} \right) \delta_{\sigma,1} + \left(\frac{1 - m_i}{2} \right) \delta_{\sigma,-1} \right) \qquad (3.23)$$

where $\delta_{a,b}$ is the Kronecker delta function and P is clearly normalized. The factorization of the probability implies a mutual independence of the statistical averages. Thus the expectations value is a simple product of each individual spins probability

$$\langle g_1\left(\sigma_1\right) g_2\left(\sigma_2\right)\rangle = \langle g_1\left(\sigma_1\right)\rangle \langle g_2\left(\sigma_2\right)\rangle \tag{3.24}$$

$$\langle g\left(\sigma_i\right)\rangle = \left(\frac{1+m_i}{2}\right)\delta_{\sigma,1} + \left(\frac{1-m_i}{2}\right)\delta_{\sigma,-1} \tag{3.25}$$

where g is an arbitrary function, left for us to choose. Substituting $g = \sigma_i$, we obtain

$$\langle \sigma_i\rangle = m_i \tag{3.26}$$

Substituting $g = H$, we obtain

$$\langle H\rangle = m_i\Lambda_{ij}m_j \tag{3.27}$$

where Λ_{ij} is a matrix defining all pairwise interactions between spins σ_i and σ_j. By substituting $g = \ln\left(P\left(S\right)\right)$ we can obtain the entropy as

$$S\left[P\right] = -\sum_i \langle \ln\left(P_i(\sigma_i)\right)\rangle = \sum_i -s\left(m_i\right) \tag{3.28}$$

where

$$s\left(m\right) \equiv \left(\frac{1+M}{2}\right)\ln\left(\frac{1+m}{2}\right) + \left(\frac{1-M}{2}\right)\ln\left(\frac{1-m}{2}\right) \tag{3.29}$$

Thus we have each ingredient present to calculate the Helmholtz free-energy defined as

$$\mathcal{A} = \langle H\rangle - \frac{S\left[P\right]}{\beta}. \tag{3.30}$$

The equilibration configuration of this system is obtained by solving for the necessary requirement $\partial\mathcal{A}/\partial m_i = 0$, which when performed, gives the set of self-consistent equations

$$m_i = \tanh\left(\beta\sum_j \Lambda_{ij}m_j\right). \tag{3.31}$$

Thus we have replace our discrete Ising spins σ_i with a continuous representation of their statistical average m_i This equation can be solved by starting in a given configuration $\{m\}$, with $m_i \sim 0$, and iteratively updated until converged as shown in Fig. 3.7(a).

   In practice, when iteratively updating that system of equations, one has to be careful with how Λ_{ij} is tuned. While D_{nn} and J_{nn} remain fixed, the value of the $|\boldsymbol{B}|$ remains to be set and will affect the slope of the hyperbolic tangent near the origin. If $|\boldsymbol{B}|$ is too large, we expect the spins to order very quickly as the hyperbolic tangent emulates a sign function as shown in Fig. 3.7 (b). The optimal $|\boldsymbol{B}|$ parameters for MFT calculations of DKSI will be discussed at the end of Chapt. 4.

(a)   (b)
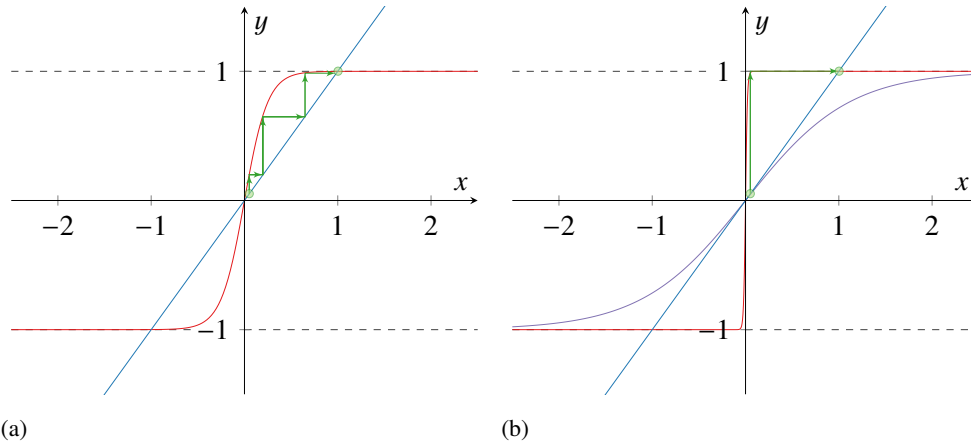
Figure 3.7: Illustration of the iterative process in updating the MFT Eq. 3.31, for a constant field, shown by the green line. In case (a), the field is sufficiently weak that the slope is determined by the local dipolar field which has a moderate slope allowing time for proper convergence of the system. As shown in (b), if the applied field dominates the local field contribution the Ising values immediately converge determined by their sign. The case of a paramagnet indicated in purple, corresponds to the temperature reducing the slope until no non trivial ($m_i = 0, \forall\, i$) solutions exist.

3.4 CHAPTER SUMMARY

This concludes the chapter dedicated to outlining the numerical techniques used in this work. A brief history of the loop move was given, originating from discussions of minimal plaquette configurations and their generalized loop counterparts. Arguments for the validity of the ergodicity and detailed balance of loop moves were provided and subsequently used to prove the ergodicity and detailed balance of kagome loop moves – loop moves restricted to individual kagome planes – in the DKSI regime. A physical motivation for the Ewald method was provided for a general unit cell and translational vectors, leaving a detailed discussion of its implementation left to Appendix. B. The benefits of non-conventional cubic unit cells for DKSI was discussed and two alternative unit cells were presented. Finally, a derivation of the self-consistent MFT equations were provided.

Part III

RESULTS, FUTURE RESEARCH & CONCLUSION

In this Part, we apply the techniques described in Chapter. 3 to the case of DKSI. We begin by presenting evidence on the nature of ordering in DKSI, describing the state, observed magnetic properties and define an order parameter. However, the clarity of this story will become *significantly* more nuanced when considering finite size effects and metastable states. An outline of the metastable states and the evidence of ergodicity breakdown in kagome loops in DKSI is presented. Calculations attempting to quantify this competition are provided by considering energy crossings and physical elongation of the unit cell. MFT calculations which support the MC results are given, while addressing the limitations of such calculations.

It will become clear that this work opens up at least as many questions as it answers and the full story of DKSI has yet to be understood. We outline prospective future research left to understand this state through relations of other closely related systems and provide some rudimentary observations. Of special interest will be the aforementioned 7-state as well as a relatively new compound known as tripod kagome ice. Finally, a conclusion is provided, highlighting the crucial results and new problems identified during this work.

4

ORDERING IN DIPOLAR KAGOME SPIN ICE

4.1 SPECIFIC HEAT & ENERGY

A good indication of a first order transition present in the system is a discontinuity in the energy at a critical temperature T_c. As $T \rightarrow T_c$, the system develops correlations as portions arrange themselves into increasingly ordered configurations which minimize the Helmholtz free-energy. At T_c, the system spontaneously breaks symmetry as spins order into a configuration which minimizes the Helmholtz free-energy better than the full set of possible states with higher entropy. It is often useful to quantify this ordering process by measuring the fluctuations present in the system. To do this, we measure the specific heat capacity C, which is defined as the variance in energy as shown in Eq. 3.7, where a discontinuous drop in the energy results in a sharp peak present in the specific heat. A sharp first order-like peak in the specific heat is observed near $T_c \sim 0.11$K in simulations of a $[4,4]_{\text{hex}}^{36}$ system, as shown in Fig. 4.1(a). The remaining portion of this chapter is dedicated to quantifying the ordered state and the set of metastable states which compete against it. A discussion drawing on all the results presented in this chapter and the nature of the ordered state is left to Sec. 5.1, in the context of the future work.

4.2 THE S-STATE AND & THE $\langle z^3 \rangle$ ORDER PARAMETER

4.2.1 *The S-state*

A systematic search for the long range ordered state was conducted as follows:

(a) Specific Heat   (b) Energy
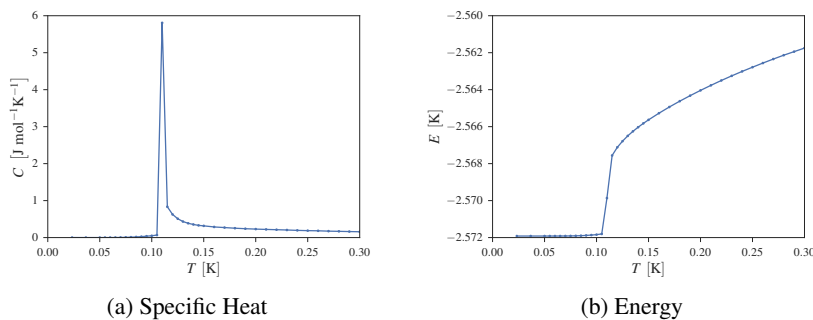
Figure 4.1: Simulations of DKSI using a $[4,4]_{\text{Hex}}^{36}$, $N = 2304$ system in an applied field of $|\boldsymbol{B}| = 0.5$ T The discontinuity in the energy and corresponding sharp peak in the specific heat strongly suggests the presence of a first order transition.
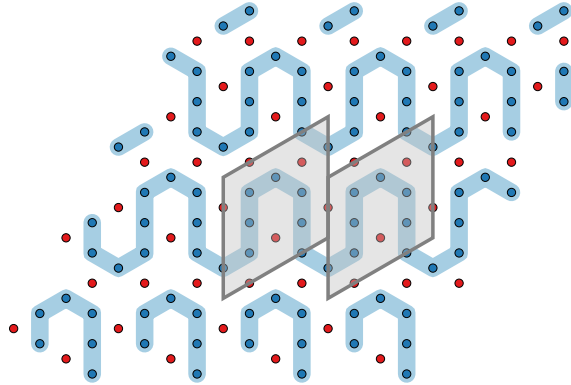
Figure 4.2: The S-state: a kagome plane slice of the ground state of DKSI, with blue and red spins respectively showing majority and minority spins which point along or against the field direction. Continuous chains of majority spins have been highlighted to show meandering "S" pattern of the state which tiles the plane in a rectilinear fashion. Two shaded cells have been provided to illustrate the magnetic unit cells and the rectangular translation vectors.

1. Generate a system configuration using one of the 3 unit cells described in Sec. 3.2.1.

2. Submit 100 MC simulations beginning in a random high temperature state

3. Cool the system gradually using 10^5 MCS for each temperature point discarding $10^{\%}$ initial MCS to allow equilibration

4. Catalogue the energy and corresponding state configurations.

Over the numerous system sizes tested, one magnetically ordered state in particular was consistently found to have the lowest lying energy. This ordered state was commensurate with system configurations of $[4n, 2m]^{36}_{\text{hex}}$, $[4n, 2m]^{12}_{\text{hex}}$, $[2n, 2m]_{\text{cube}}$.

Visual inspection of this low temperature magnetically ordered state reveals a peculiar pattern with a 16-site magnetic unit cell, arranged in the thermally active kagome planes as illustrated in Fig. 4.2. A discussion of how these planes stack along the [111] axis is left to Appendix C. Due to the nature of these spins squiggling, snaking, swerving or otherwise slithering across the plane, we simply refer to it as the *S-state*. Each kagome plane has a threefold symmetry where the S-state is rectilinearly tiled along one of three directions. By inspection of the magnetic unit cell in Fig. 4.2, one can see the Ising values of the kagome plane moments given in App. A do not fully cancel leading to a non-zero transverse magnetization of

$$
\begin{aligned}
|\boldsymbol{m}_\perp| &= \frac{1}{16} \left| (1,1,0) \cdot \sum_i \mu_i \sigma_i \right| \\
&= \frac{1}{16} \frac{\sqrt{2}}{3} \left| (2\hat{a})(2-2) + \left(-\hat{a}+\hat{b}\right)(1-3) + \left(-\hat{a}+\hat{b}\right)(1-3) \right| \\
&= \frac{\sqrt{2}}{12}
\end{aligned}
\tag{4.1}
$$
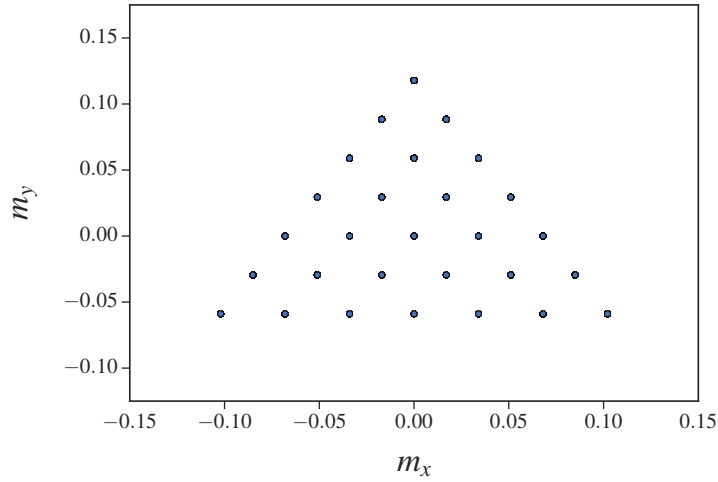
Figure 4.3: Distribution of the magnetic sectors in DKSI. An MC simulation using a system configuration of $[4, 2]^{12}_{\text{Hex}}$ was cooled to $T \sim 0.15$ K and the magnetization of each state was plotted. The triangular grid is a byproduct of kagome ice rules and the specific threefold orientation of spanning loops allowed to change the magnetization.

The observed $m_\perp$ magnetization values of DKSI form a triangular grid, as shown in Fig. 4.3. The triangular grid arrangement of the magnetizations is a result of the kagome ice rules severely restricting the seemingly continuous choices of magnetizations present in the paramagnetic phase. Each of these points on the grid is said to be a *magnetic sector*, a subset of the kagome ice manifold defined by a specific transverse magnetization vector. The selection of one of the magnetic sectors existing at the vertices of the triangular grid coincides with the selection of the magnetic sector of the S-state.

This effective bounding of the transverse magnetization allows us to define an order parameter exploiting the triangular grid pattern of the magnetization value. We map the magnetization values to the complex plane by setting the y-axis to the imaginary axis and the x-axis as the real axis. The values are than cubed to wrap them around the complex plane and represent deviations about the real axis. These vectors expressed as complex numbers are then averaged to give one complex value which is monitored by its absolute value. Formally, this can be expressed as

$$\left| \left\langle z^3 \right\rangle \right| = \left| \left\langle \left(\boldsymbol{m} \cdot \hat{a} + i \boldsymbol{m} \cdot \hat{b} \right)^3 \right\rangle \right| \tag{4.2}$$

where $\hat{a}$ and $\hat{b}$ are perpendicular with each other and the cubic [111] axis as shown in Fig. 3.4. Upon inspecting the order parameter, we find an extremely clear approach to discontinuities present for DKSI systems as shown in Fig. 4.4, suggesting again a transition of a first order nature.
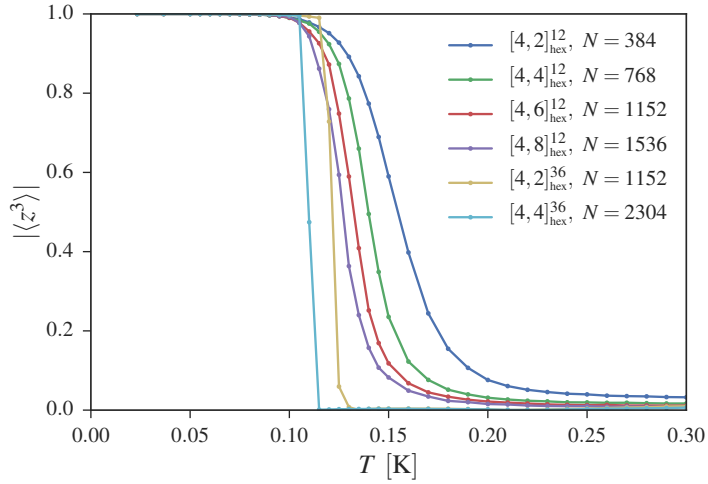
Figure 4.4: The $\langle z^3 \rangle$ order parameter applied to a variety of system sizes. As system size increases a clear discontinuity is approached near $T_c \sim 0.11$ K.

Generally, such discontinuous behaviour is accompanied by a variety of other first order transition behaviours, especially various finite size scaling arguments which, for example, dictate that the peak position in the specific heat should vary as

$$T_{\text{peak}} = T_c + cL^{-d} \qquad (4.3)$$

where d is the dimension of the lattice, c is a constant and T_c is the critical temperature [28]. However, we will observe no such evidence that this condition is met in a simple manner. Furthermore, we will find that measurements become increasingly laborious as size increases, aggravated by a set of metastable states which strongly compete with, if not altogether inhibit the formation of the S-state.

4.2.2 *Metastability: The Z-state & dS-state*

So far, we have selectively presented results from the largest system where the *S*-state has been obtained as the final state after the annealing procedure terminates. However, in many simulation runs, competing meta-stable states appear to convolute the apparent first nature of the transition. We now present results from multiple system sizes in Fig. 4.5, where three behaviours become immediately apparent and which we will address:

1. the peak in the specific heat is sometimes accompanied with a high temperature "shoulder" attached to it

2. the temperature location of the "shoulder" roughly coincides with the maxima location of small systems

3. maxima of the specific heat for system sizes of $[4, 2n]^{12}_{\text{hex}}$ do not scale monotonically
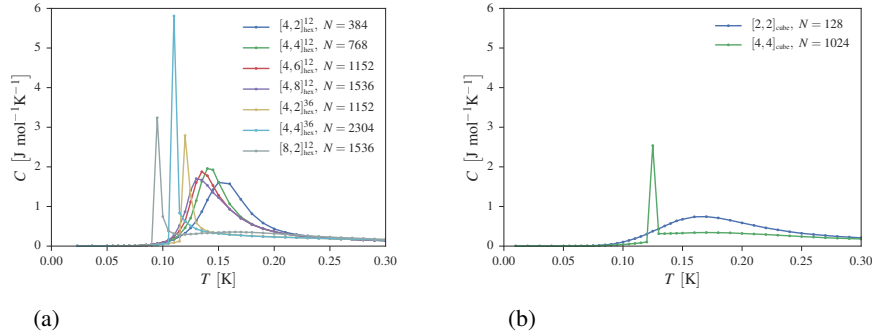
Figure 4.5: The specific heat of a variety of system sizes and geometries of DKSI. Multiple individual simulations using a variety of system configurations were cooled using 10^5 MCS. Specific heats of simulations which attained the S-state at low temperatures are shown; systems using hexagonal and cubic unit cells shown in (a) and (b), respectively. The unreliability of peak position and maxima convolute the first order transition like transition apparent in the largest simulation size shown in Fig. 4.4 indicating significant finite size effects present.

The presence of a soft maximum occurring at a slightly higher temperature than the apparent first phase transition, which we refer to as a "shoulder", indicates a build up of finite correlations just before the transition. It is interesting to note that the position of the soft maximum roughly coincides with the position of the maximum obtained in simulations using smaller system sizes such as $[2,2]_{\text{cube}}$ and $[4,2]_{\text{hex}}^{12}$. This coincidence suggests that in adequately small systems, the set of short-range correlations driving the transition into the S-state is similar to the short range correlations which manifest as the shoulder in larger systems. This reasoning may help make sense of the violation of monotonicity of the specific heat peak in the $[4,2n]_{\text{hex}}^{12}$ set of systems. If it were the intra-plane correlations that drive the transition, one would expect an increase in the height and consequently the amount of allowed inter-plane correlations, to not benefit development of the peak.

The presence of these short-range correlations developing in larger systems appear to play a significant role in the development of metastable regimes in DKSI. The minimization of the Helmholtz free-energy in these local metastable regions results in the formation of two metastable states shown in Fig. 4.6 and Fig. 4.7 referred to as the Z-state and dS-state, respectively. The defective S-state (dS-state) is perhaps the more intuitive of the two metastable states as it can be viewed as the S-state with additional low-energy insertions of the H-state. *Curiously*, the number of inserts occurring always ensures the magnetization of the S-state was exactly halved, a property which will be discussed later. Unfortunately, the dS-state was only able to be found in $[8,2]_{\text{Hex}}^{36}$ systems as probing larger simulation sizes using the 36-site unit cell is extremely cpu time costly. The next possible state to fit the dS-state would be $[8,4]_{\text{Hex}}^{36}$ ($N = 9216$), far removed from the computational reach of fully interacting dipolar systems allowing to obtain meaningful results in feasible cpu time.
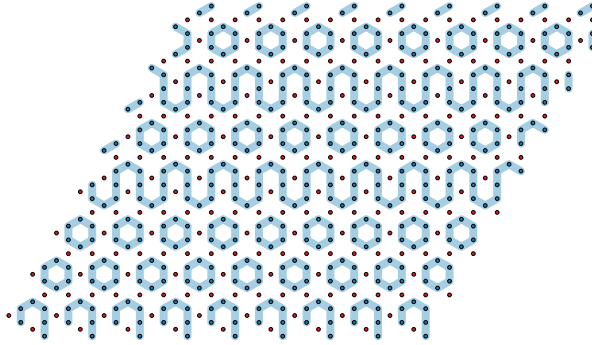
Figure 4.6: The dS-state: metastable state of DKSI composed of partial stripes of the S-state and H-state, with blue and red dots, respectively representing majority and minority spins pointing along and against the applied magnetic field. Continuous chains of majority spins have been highlighted to help illustrate the rectilinear tiling. While the H-state insertions appear in a random interspersed fashion, the presence of exactly four insertions was seen in all occurrences of simulations using $[8,2]^{36}_{\text{hex}}$ suggesting a systematic procedure into metastability.

The Z-state is formed by fragments of the S-state and H-state although this time arranged in a complex zigzagging mosaic shown in Fig. 4.7. It has a moderately sized magnetic unit cell of 128-spins and is observed in both cubic and hexagonal systems $[4,4]_{\text{cube}}$ and $[8,2]^{12}_{\text{hex}}$. Similarly to the S-state it also displays a threefold symmetry selecting a transverse magnetization equal to half of that of the S-state. Interestingly, the transverse direction of the Z-state magnetization is antiparallel with the S-state and dS-state.

To address the issues of metastability, multiple simulations were submitted in hopes a portion would escape the entrapment of the metastable regions. In the submission of 100 simulation runs started with different random seeds, the percentage of final low temperature configurations which finished in a metastable state are given in Table. 4.1. This gives little reason to expect simulations of sizes $N \gtrsim 1500$ would be able to correctly reach the S-state.

Further considerations of how systems become trapped highlight even more difficulties present in simulating DKSI. To observe all separate 100 simulations simultaneously, we plot their respective energy curves together with a transparency value, shown in Fig. 4.8. We observe clear violation of the monotonicity of the energy curve implying a

System	N	MCS	trapped
$[4,4]_{\text{Cube}}$	1024	10^5	87%
$[4,4]_{\text{Cube}}$	1024	10^6	68%
$[8,2]^{12}_{\text{Hex}}$	1536	10^5	99%

Table 4.1: Percentage of systems trapped in metastable states for simulations as a function of size/geometry and MCS.
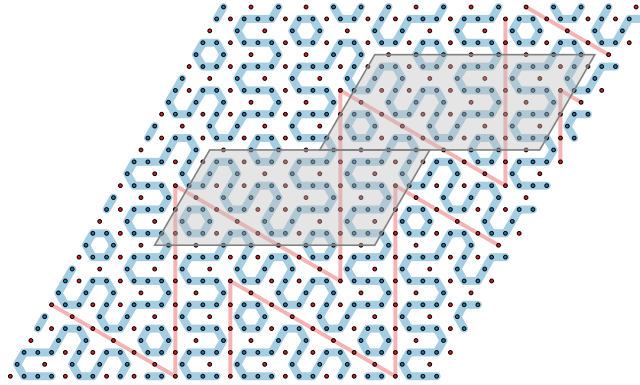
Figure 4.7: The Z-state: metastable state of DKSI composed of fragments of the S-state and H-state, with the same colouring scheme indicated in Fig. 4.6 with additional chains of minority spins highlighted to emphasize the zigzagging tessellation. Two cell has been shaded in to illustrate the magnetic unit cell and rhomboidal translational vectors.

lack of equilibration in systems despite upward values of $MCS = 10^5$ being used. Thus, despite the kagome loops being valid non-local sampling techniques, they appear to encounter problems somewhat analogous to that of single spin flip with regular DSI. That is, the kagome loop moves are too simple a sampling technique to fully navigate the extremely complex DKSI Helmholtz free-energy landscape. The specific mechanism by which this break down occurs is not yet fully understood. Additional simulations attempting to implement parallel tempering techniques did not demonstrate any benefit in helping systems avoid becoming trapped in competing states [70]. Before leaving this discussion, we dismiss a tempting possible interpretation which appears to be a reasonable argument but will be shown not to be a major deciding factor.

4.2.3 *Additional Considerations of Kagome Loops*

In the same manner of Eq. 4.1, one can derive that each metastable state exists in their own unique magnetic sector. It is tempting to assign the issues of ergodicity to the ability for kagome loops to effectively sample the magnetic sectors of the kagome ice state. As discussed in Sec. 3.1.2.3, magnetization can only change via spanning loops which utilize the boundary conditions. Thus, as system size increases we expect a decrease in the number of spanning kagome loops created, which can change $m_\perp$ and navigate the system between magnetic sectors. To quantify this, a million random loops were reversed in a $[8,2]^{36}_{\text{Hex}}$ system to quantify what the probability of creating a spanning loop in a system obeying the kagome ice rules. Out of the million random loops created $\sim 5\%$ were spanning loops suggesting the algorithmic creation of loops did not inhibit travelling between magnetic sectors.

The astute reader may argue that this result is only valid in the neighbourhood of the zero magnetic sector since the random application of loops would cancel out in a diffusive manner about zero. To quell this discussion, a series of separate systems
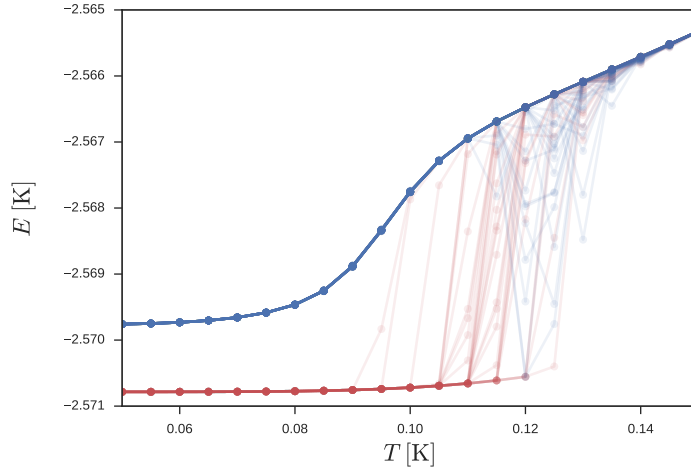
Figure 4.8: One hundred semi-transparent energy curves of DKSI for a $[4, 4]_{\text{Cube}}$ at $|\boldsymbol{B}| = 0.5$ T cooled into low temperature configurations. Blue curves indicate simulations with low temperature metastable Z-state configurations, while red curves indicate a successful transition into the S-state. Non-monotonic behaviour is observed for $T \sim 0.13$ K indicating a lack of equilibration in the systems resulting from non-ergodic kagome loops for large system sizes.

with different temperatures were initialized in a random state residing in the magnetic topological sector of the S-state. This was done by initializing a $[4, 4]_{\text{cube}}$ system in an S-state and applying 10^6 random non-spanning kagome loops to randomize the spin configuration while remaining in the S-state magnetic sector. Despite starting in the same magnetic sector as the S-state, the "shoulder" in the specific heat remained for $T > T_c$ indicating the short-range correlations were present in all magnetic sectors. These short-range correlations will be revisited and motivated at the end of this chapter.

4.2.4 *Energy Calculations*

4.2.4.1 *Field Crossings*

Given the intense competition between metastable states, it is beneficial to compare the scale of energies at which these states compete. The energy of each state can be readily calculated for various applied fields using

$$H = E_0 - g\mu_B |\boldsymbol{B}| \sum_i \left(\hat{B} \cdot \hat{z}_i \right) \sigma_i$$

$$= -m|\boldsymbol{B}| + E_0 \tag{4.4}$$

where E_0 is the energy of the Hamiltonian at zero field dependent on the nearest-neighbour exchange constant J and dipolar strength D. Clearly Eq.4.4 is linear implying

State	E_J	E_B	E_D
S-state	-1	$-1/3$	$-1.14605...$
Z-state	-1	$-1/3$	$-1.14562...$
H-state	-1	$-1/3$	$-1.14559...$
3-in/1-out	0	$-1/2$	$-0.22211...$
[001]	-1	0	$-1.16745...$
$q = X$	-1	$-1/3$	$-1.14119...$
$q = 0$	-1	$-1/3$	$-1.11387...$

Table 4.2: Ising exchange, Zeeman and dipolar energies for various states of interest.

that the energy crossings between two given states can be obtained through solving the following linear system

$$\begin{pmatrix} m^{(1)} & 1 \\ m^{(2)} & 1 \end{pmatrix} \begin{pmatrix} B_c \\ E_c \end{pmatrix} = \begin{pmatrix} E_0^{(1)} \\ E_0^{(2)} \end{pmatrix} \tag{4.5}$$

where the superscripts of (1) and (2) denote two different systems and B_c is the critical field where both systems (1) and (2) have an energy of E_c. The solution to this system can be straightforwardly solved and gives

$$B_c = \frac{E_0^{(2)} - E_0^{(1)}}{m^{(2)} - m^{(1)}} \tag{4.6}$$

It is useful to express this equation independent of the parameters J_{nn} and D_{nn} to aid in predicting critical fields of other materials. In this form we obtain

$$B_c = \frac{J\frac{1}{3}\left(E_J^{(2)} - E_J^{(1)}\right) + D\left(E_D^{(2)} - E_D^{(1)}\right)}{g\mu_B\left(E_B^{(2)} - E_B^{(1)}\right)} \tag{4.7}$$

where the Ising energy configurations of the superexchange, dipolar and Zeeman term are respectively given by E_J, E_D, E_B. While E_J and E_B can be calculated analytically, E_D still requires the use of an Ewald Matrix to properly approximate the dipolar interactions. Energies of various states of interest have been tabulated for a $[12, 12]_{\mathrm{cube}}$ system and are provided in Table. 4.2 Using Eq. 4.7 and the tabulated values, the S-state energies for various fields can calculated and plotted as shown in Fig. 4.9. The kagome ice states are predicted to be stabilized within a range of $0.02\mathrm{T} \lesssim B \lesssim 0.83\mathrm{T}$ when $T = 0$ K. A more refined inspection finds a minute difference between the S-state and the Z-state of

$$E_Z - E_S \sim 0.001 \text{ K,} \tag{4.8}$$

which is on the order of the first order-like energy gap read off of from Fig. 4.1

$$\Delta E \sim 0.005 \text{ K,} \tag{4.9}$$
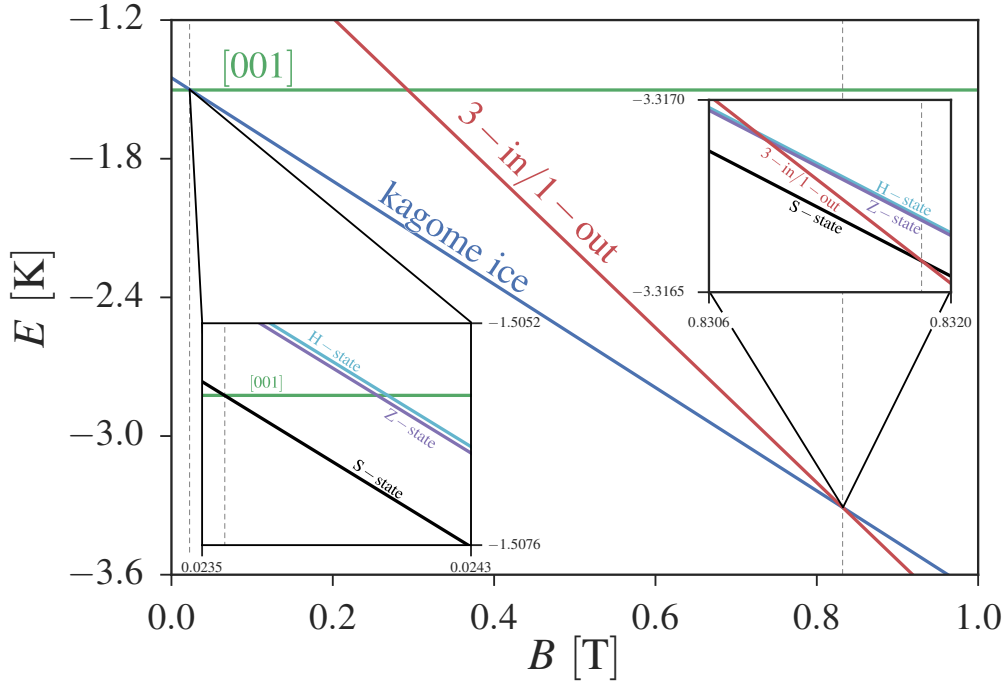
Figure 4.9: Energy plotted versus applied applied magnetic field for various states of interest with dotted lines indicating energy crossings. Insets show scale of competing ground states.

which in turn is an order less than the energy discontinuity in the zero field case of ~ 0.03 K [28] – an extremely small set of energy scales to be sampling between!

The boundaries predicted by these energy calculations were verified in MC simulations and are also consistent with previous studies of the B-T phase diagram [28, 48]. Given the evidence provided thus far, we propose the phase diagram shown in Fig. 4.10, predicting a first order phase transition between the kagome ice and S-state near $T_c \sim 0.11$ K. Unfortunately, the identification of T_c using finite-size scaling arguments is rendered moot by the competitive states which trap the system.

4.2.4.2 Elongation Calculations

Another way to compare the sensitivity of the S-state is to consider a distortion to the lattice. We introduce a parameter ϵ to tune the inter-plane spacing d, of the thermally active kagome planes perpendicular to the [111] cubic axis, as

$$d \equiv \epsilon \left(\frac{2\sqrt{6}}{3} \right) r_{\text{nn}} \tag{4.10}$$

such that when $\epsilon = 1$ the inter-plane spacing is equal to that of the pyrochlore lattice. The Ewald matrix was recalculated for a variety of ϵ values and plotted against the energy for a $[8, 4]_{\text{hex}}^{36}$ system as shown in Fig. 4.11. A value of $\epsilon \sim 1.0175$ was found
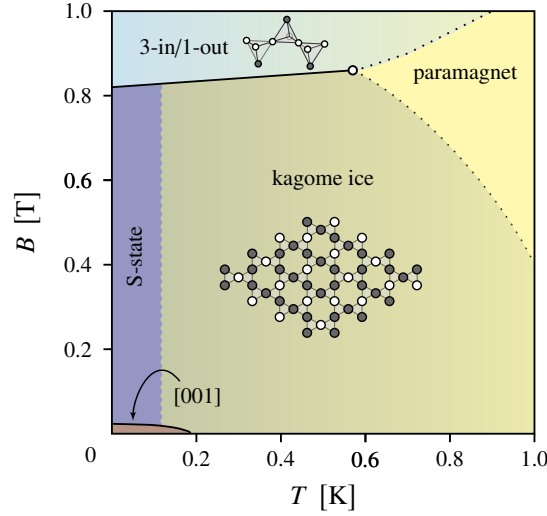
Figure 4.10: The proposed B-T phase diagram of DKSI. Solid black lines indicate the boundary of kagome ice with its neighbouring 3-in/1-out and $[001]$ states while dotted lines indicate higher temperature maximums in the specific heat leading into a triple point. The S-state is predicted to be stabilized between 0.02 T $\lesssim B \lesssim 0.83$ T and $T \lesssim 0.11$ K indicated by sharp features in the specific heat. The wavy boundary between the kagome ice and S-state indicates a region of uncertainty for the peak position. Insets have been added as examples of system configurations, with black and white dots representing inward and outward pointing spins respectively. The reader is left to refer to Fig. 4.2 and Fig. 2.1 for the S-state and 001 state, respectively.

sufficient to stabilize the H-state in the kagome planes. Interestingly, no particular translational vector was selected for stacking the H-states in the kagome planes, all translational stacking vectors calculated lead to differences in the energy within numerical error.

This result is useful in establishing contact with the related system of DKI discussed in Sec. 2.3.1 which differs by being completely two dimensional and with spin moments defined to be in-plane. However, one might suspect H-state to be a natural choice for the system to select since the charge ordering of DKI is compatible with the majority/minority ordering enforced by the pinned triangular spins in DKSI. Recall from Sec. ?? that the DKI spins are defined as *in-plane*, while for DKSI these spins point towards the center of the tetrahedron. Thus, in the limit of $\epsilon \gg r_{nn}$ at low temperatures the only difference between DKI and stretched DKSI is the moments of the kagome spins. To quantify this difference, we measure the *inclination angle* as Ω and for brevity refer to this trait as the *canting* of the kagome spins. For spins with moments pointing in-plane, such as DKI, the canting is $\Omega = 0$; for DKSI, the moments pointing towards the center of their respective tetrahedra have a canting of $\Omega \sim 20$. The canting of spins can then be viewed as a perturbation from DKI, which does not destabilize the formation of the H-state.

Figure 4.11: Energy difference of the H-state and S-state versus elongation of the system along the [111] direction. A critical elongation of value $\epsilon \sim 1.018$ indicated by dashed lines is sufficient in stabilizing the kagome plane H-state configurations in elongated DKSI.

4.3 EVIDENCE OF ORDERING FROM MEAN FIELD THEORY

Before discussing the potential future work of DKSI, it is beneficial to provide a final piece of evidence in favour of the S-state. As outlined in Sec. 3.3, an alternative to Monte Carlo simulations are MFT calculations. While MFT calculations cannot account for fluctuations unlike Monte Carlo simulations – MFT still serves as a bench mark to see if a state is stable enough to form a potential solution to a set of simple self-consistent equations. Due to the sensitive nature of MFT calculations we explicitly outline the following numerical process.

For a system of N spins indexed from $\{0, 1, \dots, N-1\}$, we define one update sweep as U when each spin in the system has been updated at least once. We define U_{tot} as the total number of update sweeps per temperature point in the simulation and U_{curr} as the current number of sweeps performed for a given temperature point. The system is initialized at a high temperature such as $T = 5$ K in a random state with spin values determined as perturbations about 0. For example $m_i = \mathtt{rand(-0.01,0.01)}$ $\forall i$ where $\mathtt{rand(-0.01,0.01)}$ generates a random number uniformly between $(-0.01, 0.01)$. The following algorithm is then executed:

1. Shuffle the index values of each spin into an array `R` and set `i=0`. For example if `N=4`, one possible shuffle is `R=[1,0,3,2]`, and the value of `R[2]` is `3`.

2. Update the current value of $m_{\mathtt{R[i]}}$ using Eq. 3.31.

3. Update the local fields of all other spins in the system.

4. If `i!=`N go to (2), else: proceed.
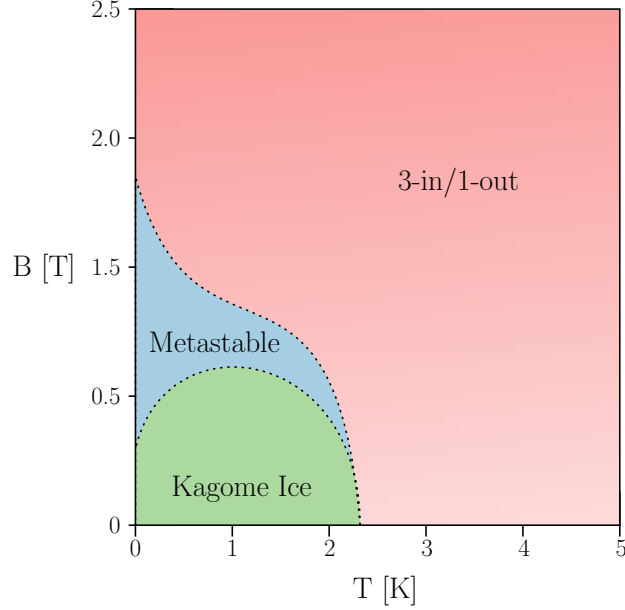
Figure 4.12: Schematic of the B-T phase diagram of MFT calculations, defining three regions: kagome ice, 3-in/1-out, and metastable. Because the MFT state cannot encapsulate fluctuations, the paramagnetic state is represented by a 3-in/1-out configuration where $m_i \sim 0 \ \forall i$ as indicated by the light red near $B \sim 0$. At moderately low temperature and field indicated in green, the MFT equations are solved by kagome ice state spin configurations, while sufficiently high temperatures and low fields result in the equations converging to a 3-in/1-out spin configuration. A region of metastability with history dependance exists between the two states indicated in blue predicting a transition of $B_c \sim 0.6$ T if simulations are simply cooled down from high temperature.

5. If $U_{\mathrm{curr}} < U_{\mathrm{tot}}$ go to (1), else: proceed.

6. Lower temperature and go to (1) until the final temperature point is met.

Using this procedure, the S-state was successfully reproduced in MFT calculations using $[4, 2]_{\mathrm{hex}}^{36}$ systems, with initial Ising values randomly perturbed about zero and cooled down from an initial temperature of 5K with an applied field between $0.015\,\mathrm{T} \lesssim |B| \lesssim 0.03$ T. Interestingly, these values correspond fairly close to the predicted critical field boundary between the [001] state and S-state, indicating the S-state is also very sensitive in MFT calculations.

As motivated in Chapt. 3, moderate fields greater than $|B| \gtrsim 0.03$ K resulted in a rapid incorrect convergence of spin values either predicting random DKSI states or the 3-in/1-out state. A critical field of $B_c \sim 0.6$ T between the S-state and 3-in/1-out state was found in direct contradiction with energetics calculation. This contradiction is

resolved through consideration of metastability in MFT calculations, where hysteresis curves generated by sequentially cooling the temperature and then raising the field or vice versa are monitored. By measuring the magnetization of the hysteresis curves a metastable region can be mapped out where the convergence of the state has a strong history dependence. As the system is cooled because the MFT calculation cannot correctly encapsulate fluctuations the paramagnetic state consists of small but non-zero Ising values in the configuration of 3-in/1-out, it tends to enter the metastable region in the 3-in/1-out state as shown in Fig. 4.12. Since the positive/negative values of the signs of spins in the paramagnetic and 3-in/1-out regime are identical, simply cooling the simulation into the metastable regime from the paramagnetic phase will falsely predict a critical field of $B_c = 0.6$ T While the MFT calculations provides a somewhat fragile description of DKSI, it is reassuring to see the stabilization of the S-state reproduced in such a simple representation of the model.

4.4 FINAL COMMENTS ON METASTABILITY AND COMPETITION

While MC simulations, MFT calculations and direct energy calculations have provided evidence of the S-state being the ground state of DKSI, a firm understanding of the competition in DKSI remains unknown. Simulations using system sizes commensurate with competitive states are accompanied by a "shoulder" in the specific heat above T_c. The soft nature of this shoulder indicates a preference for short range correlations at a higher temperature, which appear to inhibit the development of long range order. While the mechanism of this is still unknown we propose the

4.5 CHAPTER SUMMARY

In this chapter we provided evidence for the formation of an ordered ground state in DKSI existing in moderate fields between 0.02 T $\lesssim |B| \lesssim$ 0.83 T. While strongly suggestive evidence indicative of a first order transition exists, significant finite sized effects and metastable considerations convolute our understanding on the nature of the transition. The culprit competing states and their properties have been outlined and their effectiveness in trapping the simulations has been quantified. Clear evidence is provided linking the ergodic breakdown of loops to these competitive states and a tempting interpretation of this breakdown is dismissed. An attempt to quantify the sensitivity of the ordered state is provided by weakening the inter-plane interactions through elongated stretching of the lattice. We find slight perturbations of the elongation result in a stabilization of the H-state in the kagome planes with no preferential stacking configuration. A final supporting piece of evidence is provided from MFT calculations and a discussion of their limitations is provided. Taking into consideration all the evidence a proposed B-T phase diagram is presented for DKSI in Fig. 4.10.

5

PROSPECTIVE FUTURE RESEARCH

5.1 THE RELATION BETWEEN THE 7-STATE AND THE S-STATE

The presence of a transverse magnetization and unusual features in the specific heat suggest the competition between inter/intra-plane interactions are non-trivial. An interesting question arises in addressing what one ought to mean by *inter* and *intra*-plane interactions. Thus far, we have labelled intra-plane interactions, as between spins residing in the thermally relevant kagome planes as $T \to 0$ and the inter-plane interactions, for spins existing in different thermally active kagome planes. However, one can ask why these [111] *perpendicular kagome plane* (PKPs) have been the only planes viewed to understanding the dipolar ordering. The pyrochlore lattice can be decomposed into three other *slanted kagome planes* (SKPs) as shown in Fig. 5.1. Given each kagome plane still has an equivalent set of interactions, one can ask how the S-state minimizes the energy in these planes. Viewing the SKPs of the S-state reveals a remarkable observation: of the three SKPs one shows the same Ising configuration as the 7-state the previously mentioned DKA ground state in Sec. 2.3.2 [56]! This discovery of a previously identified configuration in the SKPs of the S-state raises a number of interesting questions

1. Is there any significance between 2D charge ordering and competitive DKSI configurations?

2. Could the metastability be better understood by studying the dynamics of the SKPs?

(a)   (b)   (c)   (d)

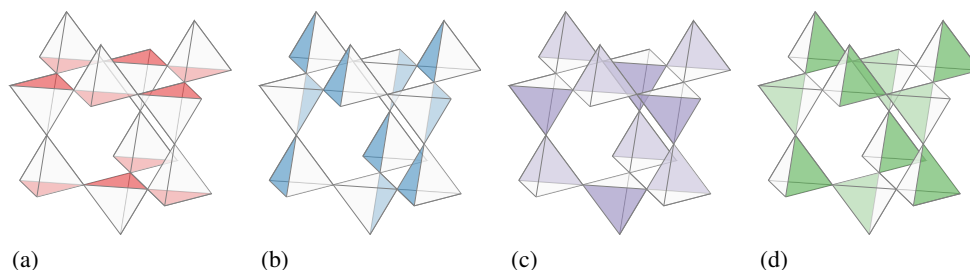Figure 5.1: Kagome plane slicings of the pyrochlore lattice. The PKP which has been predominantly used to study the S-state thus far is shown in (a). The SKPs are shown in (b), (c) and (d) each corresponding to the kagome planes which can host the same Ising configuration as the 7-state. The three fold symmetry present in the S-state is equivalent to the selection of one of the SKPs seleting the 7-state Ising configuration.
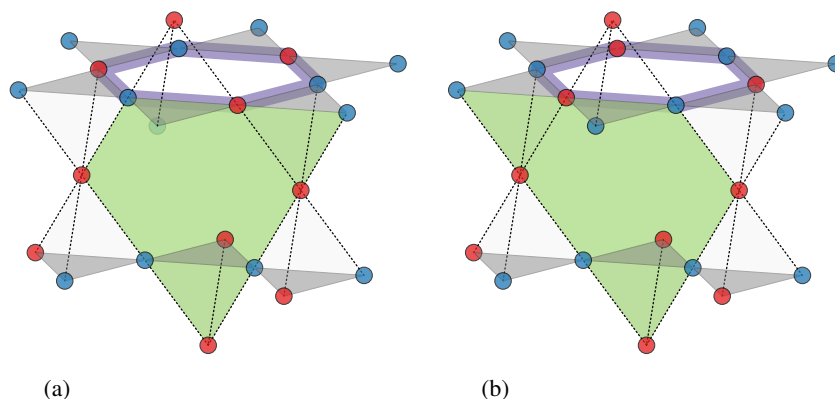
(a)   (b)

Figure 5.2: An example of two kagome ice state differing by the reversal of a hexagaonal plaque-
tte highlighted in purple. Ising values are denoted by red and blue dots as $\{+1, -1\}$
respectively. The reversal of the plaquette results in no change of the number of mi-
nority spins on triangles present in the shaded kagome planes. However, in the SKP
plane shown in Fig. 5.1 (c) the move is equivalent to the $2 \leftrightarrow 3$ swap shown in
Fig. 2.11 (b), demonstrating the DKA clustering techniques discussed in Sec. 2.3.2
may be realizable in DKSI.

3. Is the potential clustering move proposed for the 7-state applicable to overcoming
the metastable states present in DKSI?

Here we briefly discuss the third question, suggesting the potential clustering algo-
rithm proposed by Chioar *et al.* may be of use in reaching the S-state. Consider the
change in an SKP plane given the reversal of a plaquette, as shown in Fig. 5.2, where
we have highlighted the trapezoidal Ising configuration discussed in Sec. 2.3.2. Given a
loop move, we see that the equivalent 2D thermal excitation is equivalent to the $2 \leftrightarrow 3$
spin swap proposed by Chioar *et al.* which results in a reorientated trapezoid. Given one
of the energetically favourable spin swaps, is possible in DKSI via loop moves, it leaves
open the possibility of an extended cluster method for DKSI based on the proposed
clustering algorithms for DKA.

5.2   TILTED [111] FIELD & FURTHER NEIGHBOUR CORRECTIONS

Of experimental interest, one can ask if any novel physics occurs for a slight tilt in
the [111] field by some angle Ω. Recent work by Kao *et al.* [71] suggest the stabi-
lization of the $q = X$ ordered state consistent with the limit where $\phi \rightarrow \pi$ if tilted
towards one of the cubic [110] edges. Their work is consistent with experimental ob-
servations on the spin ice system $Ho_2Ti_2O_7$ [72]. However, simulations performed by
Kao *et al.* considered simulations of a $[5, 5]_{cube}$ cell which is incommensurate with
the S-state.Preliminary calculations of the ground states stabilized as a function of field
strength and deviation angle ϕ along the $[\bar{1}\bar{1}2]$ direction show the S-sate continues to
be stabilized due to the transverse magnetization before the $q = X$ state predicted in
Ref. [71]. If the tilt is along the $[11\bar{2}]$ direction, the S-sate is destabilized resulting in

Figure 5.3: A schematic phase diagram of the ground states stabilized as a function of field strength and tilt along the $[\bar{1}\bar{1}2]$ direction. The diagram compares the various states presented in Chapt. 4, using the DSI Hamiltonian Eq. 1.5 with the $Dy_2Ti_2O_7$ parameters. As the angle deviates from the $[111]$ axis the S-state is either stabilized or destabilized into the Z-state depending on the sign of the tile. In the limit of large tilt, the $q = X$ and $q = 0$ state are stabilized as their configurations saturate spins in the field direction as beneficially as possible.

the Z-state as an *intermediate* phase before the expected $q = 0$ state. It is interesting to note the existences of triple points in each case of the tilt direction. These triple points are a unique part of phase space where the Zeeman, dipolar and exchange interactions are all competitive within the Hamiltonian. A complete mapping of the phase diagram for all spherical angles, cataloguing the boundaries between states would be useful for completeness of the DSI Hamiltonian – or perhaps more wishfully – lead to the discovery of new dipolar orderings for specific field strengths and tilting.

Whether or not these destabilizing angles are relevant in experimental work remains a subject of future research. While we seem to have captured some of the more fundamental elements of DKSI such as the selection of a transverse magnetization – the influence of further nearest-neighbour corrections is still not know at this time. Any future work regarding the tilt in the context of experimental motivation should continue to keep these refinements in mind.

5.3 RELATED PHYSICALLY REALIZABLE KAGOME SYSTEMS

We end this section with a discussion of physically realizable systems with a low temperature physics seemingly related to that of DKSI. One compound of potential interest recently discovered are the tripod kagome lattices (TKLs) [73], with chemical formula with $Mg_2RE_3Sb_3O_{14}$ or $Zn_2RE_3Sb_3O_{14}$, where RE is a rare earth ion such as Gd, Er, Dy,

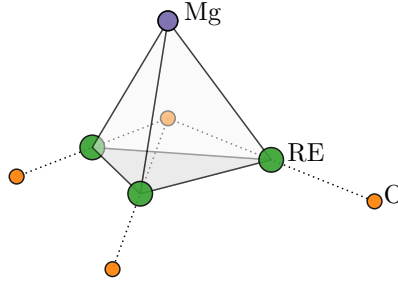Figure 5.4: Figure recreated from Ref. [73]. Configuration of atoms for an individual tripod in TKL. The non-magnetic Mg^{2+}/Zn^{2+} residing at the purple triangular site removes the internal field of present in DKSI acting on the three green kagome sites. The dashed lines indicate an axis between two oxygen atoms which is pependicular to the plane of a puckered ring of oxygens similar to that of DKSI forcing an easy Ising axis for the case of RE = Dy^{3+} [73].

shown in Fig. 5.4. TKL mimics the alternating kagome and triangular planes present in DKSI by creating kagome layers of rare earths and triangular layers of non-magnetic Mg^{2+}/Zn^{2+} ions. Of these rare earths, the Dy^{3+} ion with an effective spin-1/2 Kramers ion is surrounded by an oxygen cage, and similar to the DSI case proposed to be Ising-like with moments in the directions [73]. Thus TKL is expected to obey the same set of 2-in, 1-out kagome ice rules as DKSI with three key differences, that we now discuss.

Firstly, in the case of DKSI, the magnetic field pins the triangular spins at low temperatures creating an effective internal field that acts on the kagome layers only allowing the majority spins to point along the direction of the magnetic field. In the case of TKL in zero field, no such restriction on majority spins is placed on the kagome layers due to the non-magnetic Mg^{2+}/Zn^{2+} ions creating no internal field. This freedom in majority and minority spins makes TKL a better realization of Wills' Ice rules as opposed to DKSI. However, the moments with which the Ising axes lie along are not in plane like Wills' Ice, but instead canted with respect to the kagome planes by an angle of $\sim 28°$ as opposed to the $\sim 20°$ canting of the pyrochlore case [70]. Still, the number of allowed states in TKL is enormously larger than that of DKSI possibly allowing the formation of intermediate states, which may aid in guiding the system to find the S-state or previously unknown configurations. Furthermore, the replacement of the triangular layers with Mg^{2+} ions leads to a shrinking of the inter-plane difference approximately equal to $\epsilon \sim 0.964$ [70]. Given a deformation of the lattice of approximately $\epsilon \sim 1.0175$ is enough to destabilize the S-state into the H-state, as shown in Sec. 4.2.4.2; this material is well within the range where possible alterations to the lattice may stabilize an ordered state other than the S-state.

Work on these compounds has recently begun [73, 74], presenting experimental results suggesting a staggered charge order established in line with the work of Chern *et al.* [53]. This charge ordering represents a physical process in TKL not physically possible in DKSI where charge is everywhere zero due to the rare earth nature of triangular sites. However, every configuration of DKSI has a corresponding configuration in TKL,

providing a set of states to begin looking for the possible presence of in the TKL system. Thus, it is possible that the S-state could manifest itself in the TKL system.

While the DKSI and TKL systems do differ by application of magnetic field and canting of the spins, it is still instructive to consider the case of DKSI with the same interplane spacing as TKL. Preliminary work shows that a slight compression of $\epsilon \sim 0.964$ of the interplane spacing results in a further stabilization of the S-state. However, a proper prediction of the S-state will require the proper implementation of Ising moments, interplane spacing and removal of magnetic triangular sites.

5.4 CHAPTER SUMMARY

In this chapter we have discussed three prospective topics of future research. Of theoretical interest, we related the S-state to the previously studied two-dimensional model of DKA [56], which also experiences difficulties with equilibration. The proposed clustering method for DKA discussed in Sec. 2.3.2, is related to DKSI by demonstrating spin swap moves can be expressed as kagome loop moves. Of theoretical and experimental interest we discussed the case of a tilted [111] field and the stabilization of the S- and Z-state and proposed a phase diagram comparing field strength and tilt along the [$\bar{1}$ bar12] direction. Finally, we discuss the related system of TKL where substitution of non-magnetic Mg^{2+}/Zn^{2+} ions remove the internal fields acting on the kagome layers of DKSI. Rudimentary calculations exploring the change in inter-plane distance, suggest that the S-state would be a good ground state candidate in TKL, although a more rigorous numerical study is still required.

6

CONCLUSION

In this work we have discussed the subject of dipoles ordering in spin ice when subjected to an applied field of moderate strength along the cubic [111] axis. We used the simplest possible Hamiltonian composed of a super-exchange, Zeeman and dipolar term; to encapsulate ordering behaviour of this system, which we refered to as Dipolar Kagome Spin Ice (DKSI). While the super-exchange term can be effectively handled using a local sampling method such as a single spin flip, the sampling of minute dipolar interactions requires a non-local *kagome loop move* which tunnels between ice states. Due to a subset of spins on the pyrochlore lattice fully projecting onto the [111] field, the pyrochlore lattice decomposes into pinned triangular lattices interleaved by thermally active kagome planes. The long-range nature of the dipolar interactions were handled using the well known Ewald method. A variety of unit cells were used in simulations to account for non-trivially shaped magnetic unit cells, required to minimize the complicated set of dipolar interactions.

We found a candidate ground state, that we referred to as the S-state, which is characterized by a meandering pattern of "majority" kagome spins which point along the direction of the field. While some system sizes indicated a transition of the first order type, the certainty of this transitions was obscured by other system sizes demonstrating varying heights and location of peaks in the specific heat. This behaviour appears to be a consequence of a strong competition present in DKSI between the ground state and other competitive states. Features in the specific heat suggest this competition arises from local correlations which inhibit the development of the long range ordered state. These competitive states came in two particular configurations referred to as the Z-state and dS-state, each of which are characterized by a magnetization value exactly half that of the S-state. At a system size of $N \sim 1500$ spins we found that $\sim 99\%$ of the simulations become trapped in these competitive statse for simulations using 10^5 MCS. While increasing the amount of MCS did decrease the proportion of simulations that become trapped, the expensive nature of dipolar interactions restricted larger simulations.

We further verified the S-state through performing mean field theory (MFT) calculations which neglected fluctuations as an approximation. While the S-state was found to be a solution of the MFT self-consistent equations, it was extremely sensitive with the only observed solutions occurring for values of $|B| \sim 0.02$ T. Other field values of the strength $|B| \gtrsim 0.05$ T converged too quickly, into arbtirary kagome ice phases.

To better quantify the sensitivity of the S-state, we compared the energy values of systems elongated along the [111] cubic axis, to reduce the inter-plane correlations sufficiently to destabilize the S-state. We found a value of $\sim 2\%$ was sufficient to lead in a stabilization of a new ground state in the kagome planes, referred to as the H-state. The Ising configuration of the H-state has been observed as the ground state of a variety of two dimensional kagome systems in the past.

Finally, a discussion of future work left for studying DKSI was provided. Of theoretical interest, a relation was drawn between the S-state and previously known 7-state to propose a potential clustering move. Of equal interest experimentally and theoretically we discussed the application of a tilted [111] field and stabilization of a variety of magnetically ordered states. Additionally, we discussed a new class of related compounds referred to as tripod kagome lattices (TKL) which display a set of low temperature interactions similar to those of DKSI.

BIBLIOGRAPHY

[1] J. Vannimenus and G. Toulouse. "Theory of the frustration effect. II. Ising spins on a square lattice." In: *Journal of Physics C: Solid State Physics* 10.18 (1977), p. L537.

[2] W. H. Barnes. "The Crystal Structure of Ice between 0 degrees C. and - 183 degrees C." In: *Proceedings of the Royal Society of London A: Mathematical, Physical and Engineering Sciences* 125.799 (1929), pp. 670–693.

[3] J. D. Bernal and R. H. Fowler. "A Theory of Water and Ionic Solution, with Particular Reference to Hydrogen and Hydroxyl Ions." In: *The Journal of Chemical Physics* 1.8 (1933), pp. 515–548.

[4] W. F. Giauque and M. F. Ashley. "Molecular Rotation in Ice at $10°K$. Free Energy of Formation and Entropy of Water." In: *Phys. Rev.* 43 (1 1933), pp. 81–82.

[5] L. Pauling. "The Structure and Entropy of Ice and of Other Crystals with Some Randomness of Atomic Arrangement." In: *Journal of the American Chemical Society* 57.12 (1935), pp. 2680–2684.

[6] P. W. Anderson. "Ordering and Antiferromagnetism in Ferrites." In: *Phys. Rev.* 102 (4 1956), pp. 1008–1013.

[7] S. T. Bramwell and M. J. Harris. "Frustration in Ising-Type Spin Models on the Pyrochlore Lattice." In: *Journal of Physics: Condensed Matter* 10.14 (1998), p. L215.

[8] S. T. Bramwell and M. J. P. Gingras. "Spin Ice State in Frustrated Magnetic Pyrochlore Materials." In: *Science* 294.5546 (2001), pp. 1495–1501.

[9] M. J. Harris, S. T. Bramwell, D. F. McMorrow, T. Zeiske, and K. W. Godfrey. "Geometrical Frustration in the Ferromagnetic Pyrochlore $Ho_2Ti_2O_7$." In: *Phys. Rev. Lett.* 79 (13 1997), pp. 2554–2557.

[10] A. P. Ramirez, A. Hayashi, R. J. Cava, R. Siddharthan, and B. S. Shastry. "Zero-Point Entropy in "Spin Ice"." In: *Nature* 399.6734 (1999), pp. 333–335.

[11] R. Siddharthan, B. S. Shastry, A. P. Ramirez, A. Hayashi, R. J. Cava, and S. Rosenkranz. "Ising Pyrochlore Magnets: Low-Temperature Properties, "Ice Rules," and Beyond." In: *Phys. Rev. Lett.* 83 (9 1999), pp. 1854–1857.

[12] B. C. den Hertog and M. J. P. Gingras. "Dipolar Interactions and Origin of Spin Ice in Ising Pyrochlore Magnets." In: *Phys. Rev. Lett.* 84 (15 2000), pp. 3430–3433.

[13] R. G. Melko, B. C. den Hertog, and M. J. P. Gingras. "Long-Range Order at Low Temperatures in Dipolar Spin Ice." In: *Phys. Rev. Lett.* 87 (6 2001), p. 067203.

[14] R. G. Melko. *Low Temperature Physics of Dipolar Spin Ice: A Monte Carlo Study*. University of Waterloo, 2001.

[15] M. J. P Gingras and B. C. den Hertog. "Origin of Spin-Ice Behavior in Pyrochlore Magnets with Long-Range Dipole Interactions: an Insight from Mean-Field Theory." In: *Canadian Journal of Physics* 79.11-12 (2001), pp. 1339–1351.

[16] P. P. Ewald. "Die Berechnung Optischer und Elektrostatischer Gitterpotentiale." In: *Annalen der Physik* 369.3 (1921), pp. 253–287.

[17] S. V. Isakov, R. Moessner, and S. L. Sondhi. "Why Spin Ice Obeys the Ice Rules." In: *Phys. Rev. Lett.* 95 (21 2005), p. 217201.

[18] J. Snyder, B. G. Ueland, J. S. Slusky, H. Karunadasa, R. J. Cava, and P. Schiffer. "Low-Temperature Spin Freezing in the $Dy_2Ti_2O_7$ Spin Ice." In: *Phys. Rev. B* 69 (6 2004), p. 064414.

[19] J. Snyder, J. S. Slusky, R. J. Cava, and P. Schiffer. "How "Spin Ice" Freezes." In: *Nature* 413.6851 (2001), pp. 48–51.

[20] Ludovic D. C. Jaubert. "Topological Constraints and Defects in Spin Ice." PhD thesis. Ecole normale supérieure de lyon - ENS LYON, 2009.

[21] B. Klemke, M. Meissner, P. Strehlow, K. Kiefer, S. Grigera, and D. Tennant. "Thermal Relaxation and Heat Transport in the Spin Ice Material $Dy_2Ti_2O_7$." In: *Journal of Low Temperature Physics* 163.5-6 (2011), pp. 345–369.

[22] R. Higashinaka, H. Fukazawa, D. Yanagishima, and Y. Maeno. "Specific heat of $Dy_2Ti_2O_7$ in Magnetic Fields: Comparison Between Single-Crystalline and Polycrystalline Data." In: *Journal of Physics and Chemistry of Solids* 63.6-8 (), pp. 1043–1046.

[23] D. J. P. Morris, D. A. Tennant, S. A. Grigera, B. Klemke, C. Castelnovo, R. Moessner, C. Czternasty, M. Meissner, K. C. Rule, J. U. Hoffmann, K. Kiefer, S. Gerischer, D. Slobinsky, and R. S. Perry. "Dirac Strings and Magnetic Monopoles in the Spin Ice $Dy_2Ti_2O_7$." In: *Science* 326.5951 (2009), pp. 411–414.

[24] H. Kadowaki, N. Doi, Y. Aoki, Y. Tabata, T. J. Sato, J. W. Lynn, K. Matsuhira, and Z. Hiroi. "Observation of Magnetic Monopoles in Spin Ice." In: *Journal of the Physical Society of Japan* 78.10 (2009), p. 103706.

[25] D. Pomaranski, L. R. Yaraskavitch, S. Meng, K. A. Ross, H. M. L. Noad, H. A. Dabkowska, B. D. Gaulin, and J. B. Kycia. "Absence of Pauling's Residual Entropy in Thermally Equilibrated $Dy_2Ti_2O_7$." In: *Nat Phys* 9.6 (2013). Letter, pp. 353–356.

[26] J. G. Rau and M. J. P. Gingras. "Magnitude of Quantum effects in Classical Spin Ices." In: *Phys. Rev. B* 92 (14 2015), p. 144417.

[27] P. Henelius, T. Lin, M. Enjalran, Z. Hao, J. G. Rau, J. Altosaar, F. Flicker, T. Yavors'kii, and M. J. P. Gingras. "Refrustration and Competing Orders in the Prototypical $Dy_2Ti_2O_7$ Spin Ice Material." In: *Phys. Rev. B* 93 (2 2016), p. 024402.

[28] R. G. Melko and M. J. P. Gingras. "Monte Carlo Studies of the Dipolar Spin Ice Model." In: *Journal of Physics: Condensed Matter* 16.43 (2004), R1277.

[29] T. Fennell, O. A. Petrenko, B. Fåk, J. S. Gardner, S. T. Bramwell, and B. Ouladdiaf. "Neutron Scattering Studies of the Spin Ices $Ho_2Ti_2O_7$ and $Dy_2Ti_2O_7$ in Applied Magnetic Field." In: *Phys. Rev. B* 72 (22 2005), p. 224411.

[30] L. D. C. Jaubert, J. T. Chalker, P. C. W. Holdsworth, and R. Moessner. "Three-Dimensional Kasteleyn Transition: Spin Ice in a [100] Field." In: *Phys. Rev. Lett.* 100 (6 2008), p. 067207.

[31] L. D. C. Jaubert, J. T. Chalker, P. C. W. Holdsworth, and R. Moessner. "The Kasteleyn Transition in Three dimensions: Spin Ice in a [100] Field." In: *Journal of Physics: Conference Series* 145.1 (2009), p. 012024.

[32] J. P. C. Ruff, R. G. Melko, and M. J. P. Gingras. "Finite-Temperature Transitions in Dipolar Spin Ice in a Large Magnetic Field." In: *Phys. Rev. Lett.* 95 (9 2005), p. 097202.

[33] R. Becker. "Zur Theorie der Magnetisierungskurve." In: *Zeitschrift für Physik* 62.3 (1930), pp. 253–269.

[34] J. R. Tessman. "Magnetic Anisotropy at 0°K." In: *Phys. Rev.* 96 (5 1954), pp. 1192–1195.

[35] T. Fennell, O. A. Petrenko, B. Fåk, S. T. Bramwell, M. Enjalran, T. Yavors'kii, M. J. P. Gingras, R. G. Melko, and G. Balakrishnan. "Neutron Scattering Investigation of the Spin Ice State in $Dy_2Ti_2O_7$." In: *Phys. Rev. B* 70 (13 2004), p. 134408.

[36] H. Sato, K. Matsuhira, T. Tayama, Z. Hiroi, S. Takagi, and T. Sakakibara. "Ferromagnetic Ordering on the Triangular Lattice in the Pyrochlore Spin-Ice Compound $Dy_2Ti_2O_7$." In: *Journal of Physics: Condensed Matter* 18.22 (2006), p. L297.

[37] T. Yavors'kii, T. Fennell, M. J. P. Gingras, and S. T. Bramwell. "$Dy_2Ti_2O_7$ Spin Ice: A Test Case for Emergent Clusters in a Frustrated Magnet." In: *Phys. Rev. Lett.* 101 (3 2008), p. 037204.

[38] T. Lin. *A Study of the Effect of Perturbations in Spin Ice systems: Site Dilution, Weak Exchange, Quantum and Finite-Size Effects*. University of Waterloo, 2014.

[39] S. Yoshida, K. Nemoto, and K. Wada. "Ordered Phase of Dipolar Spin Ice under [110] Magnetic Field." In: *Journal of the Physical Society of Japan* 73.7 (2004), pp. 1619–1622.

[40] J. P. Clancy, J. P. C. Ruff, S. R. Dunsiger, Y. Zhao, H. A. Dabkowska, J. S. Gardner, Y. Qiu, J. R. D. Copley, T. Jenkins, and B. D. Gaulin. "Revisiting Static and Dynamic Spin-Ice Correlations in $Ho_2Ti_2O_7$ with Neutron Scattering." In: *Phys. Rev. B* 79 (1 2009), p. 014408.

[41] H. Fukazawa, R. G. Melko, R. Higashinaka, Y. Maeno, and M. J. P. Gingras. "Magnetic Anisotropy of the Spin-Ice Compound $Dy_2Ti_2O_7$." In: *Phys. Rev. B* 65 (5 2002), p. 054410.

[42] M. J. Harris, S. T. Bramwell, P. C. W. Holdsworth, and J. D. M. Champion. "Liquid-Gas Critical Behavior in a Frustrated Pyrochlore Ferromagnet." In: *Phys. Rev. Lett.* 81 (20 1998), pp. 4496–4499.

[43] O. A. Petrenko, M. R. Lees, and G. Balakrishnan. "Magnetization Process in the Spin-Ice Compound $Ho_2Ti_2O_7$." In: *Phys. Rev. B* 68 (1 2003), p. 012406.

[44] K. Matsuhira, Z. Hiroi, T. Tayama, S. Takagi, and T. Sakakibara. "A New Macroscopically Degenerate Ground State in the Spin Ice Compound $Dy_2Ti_2O_7$ Under a Magnetic Field." In: *Journal of Physics: Condensed Matter* 14.29 (2002), p. L559.

[45] T. Sakakibara, T. Tayama, Z. Hiroi, K. Matsuhira, and S. Takagi. "Observation of a Liquid-Gas-Type Transition in the Pyrochlore Spin Ice Compound $Dy_2Ti_2O_7$ in a Magnetic Field." In: *Phys. Rev. Lett.* 90 (20 2003), p. 207205.

[46] R. Moessner and S. L. Sondhi. "Theory of the [111] Magnetization Plateau in Spin Ice." In: *Phys. Rev. B* 68 (6 2003), p. 064411.

[47] S. V. Isakov, K. S. Raman, R. Moessner, and S. L. Sondhi. "Magnetization Curve of Spin Ice in a [111] Magnetic Field." In: *Phys. Rev. B* 70 (10 2004), p. 104418.

[48] C. Castelnovo, R. Moessner, and S. L. Sondhi. "Magnetic Monopoles in Spin Ice." In: *Nature* 451.7174 (2008), pp. 42–45.

[49] J. Hamp, A. Chandran, R. Moessner, and C. Castelnovo. "Emergent Coulombic Criticality and Kibble-Zurek Scaling in a Topological Magnet." In: *Phys. Rev. B* 92 (7 2015), p. 075142.

[50] A. S. Wills, R. Ballou, and C. Lacroix. "Model of Localized Highly Frustrated Ferromagnetism: The *Kagome* Spin Ice." In: *Phys. Rev. B* 66 (14 2002), p. 144407.

[51] T. Takagi and M. Mekata. "Magnetic Ordering of Ising Spins on Kagome Lattice with the 1st and the 2nd Neighbor Interactions." In: *Journal of the Physical Society of Japan* 62.11 (1993), pp. 3943–3953.

[52] M. Wolf and K. D. Schotte. "Ising Model with Competing Next-Nearest-Neighbour Interactions on the Kagome Lattice." In: *Journal of Physics A: Mathematical and General* 21.9 (1988), p. 2195.

[53] G. Chern and O. Tchernyshyov. "Magnetic Charge and Ordering in Kagome Spin Ice." In: 370.1981 (2012), pp. 5718–5737.

[54] J. L. Cardy. "General Discrete Planar Models in Two Dimensions: Duality Properties and Phase Diagrams." In: *Journal of Physics A: Mathematical and General* 13.4 (1980), p. 1507.

[55] H. Otsuka. "Monomer-Dimer Mixture on a Honeycomb Lattice." In: *Phys. Rev. Lett.* 106 (22 2011), p. 227204.

[56] I. A. Chioar, N. Rougemaille, and B. Canals. "Ground-State Candidate for the Classical Dipolar Kagome Ising Antiferromagnet." In: *Phys. Rev. B* 93 (21 2016), p. 214410.

[57] Kendall E Atkinson. *An introduction to numerical analysis*. John Wiley & Sons: Hoboken, New Jersey, 2008.

[58] M. E. J. Newman and G. T. Barkema. *Monte Carlo Methods in Statistical Physics chapter 1-4*. Oxford University Press: New York, USA, 1999.

[59] C. Andrieu, N. De Freitas, A. Doucet, and M. I. Jordan. "An Introduction to MCMC for Machine Learning." In: *Machine learning* 50.1-2 (2003), pp. 5–43.

[60] C. Robert and G. Casella. *Monte Carlo Statistical Methods*. Springer Science & Business Media: Springer-Verlag New York, 2013.

[61] H. G. Katzgraber. "Introduction to Monte Carlo Methods." In: *arXiv preprint arXiv:0905.1629* (2009).

[62] R. Siddharthan, B. S. Shastry, and A. P. Ramirez. "Spin Ordering and Partial Ordering in Holmium Titanate and Related Systems." In: *Phys. Rev. B* 63 (18 2001), p. 184412.

[63] Andrew J Macdonald, Peter C W Holdsworth, and Roger G Melko. "Classical topological order in kagome ice." In: *Journal of Physics: Condensed Matter* 23.16 (2011), p. 164208.

[64] M. P. Allen and D. J. Tildesley. *Computer Simulation of Liquids*. Oxford university press, 1989.

[65] Z. Wang and C. Holm. "Estimate of the Cutoff Errors in the Ewald Summation for Dipolar Systems." In: *The Journal of Chemical Physics* 115.14 (2001), pp. 6351–6359.

[66] S. W. De Leeuw, J. W. Perram, and E. R. Smith. "Computer Simulation of the Static Dielectric Constant of Systems with Permanent Electric Dipoles." In: *Annual review of physical chemistry* 37.1 (1986), pp. 245–270.

[67] D. M. Heyes. "Electrostatic Potentials and Fields in Infinite Point Charge Lattices." In: *The Journal of Chemical Physics* 74.3 (1981), pp. 1924–1929.

[68] F. Berthaut. "L'Énergie Électrostatique de Reseaux Ioniques." In: *J. phys. radium* 13.11 (1952), pp. 499–505.

[69] G. Parisi. *Statistical Field Theory*. Advanced book classics. Perseus Books: New York, USA, 1998.

[70] J. G. Rau. *(private communication)*.

[71] W. Kao, P. C. W. Holdsworth, and Y. Kao. "Field-Induced Ordering in Dipolar Spin Ice." In: *Phys. Rev. B* 93 (18 2016), p. 180410.

[72] T. Fennell, S. T. Bramwell, D. F. McMorrow, P. Manuel, and A. R. Wildes. "Pinch Points and Kasteleyn Transitions in Kagome Ice." In: *Nat Phys* 3.8 (2007), pp. 566–572.

[73] Z. L. Dun, J. Trinh, K. Li, M. Lee, K. W. Chen, R. Baumbach, Y. F. Hu, Y. X. Wang, E. S. Choi, B. S. Shastry, A. P. Ramirez, and H. D. Zhou. "Magnetic Ground States of the Rare-Earth Tripod Kagome Lattice $Mg_2RE_3Sb_3O_{14}$ (RE = Gd, Dy, Er)." In: *Phys. Rev. Lett.* 116 (15 2016), p. 157201.

[74] J. A. M. Paddison, H. S. Ong, J. O. Hamp, P. Mukherjee, X. Bai, M. G. Tucker, N. P. Butch, C. Castelnovo, M. Mourigal, and S. E. Dutton. *Emergent Order in the Kagome Ising Magnet* $Dy_3Mg_2Sb_3O_{14}$. 2016.

A

APPENDIX A: THE PYROCHLORE LATTICE

When working with spin ice, it is important to have a strong understanding of the pyrochlore lattice. Discussions of alternating layers, ABC stacking, PKP/SKP slices, orientations of moments and stacking vectors become overwhelming quite quickly, without the definitions explicitly tabulated. In this appendix, we provide tables for the benefit of the reader who wishes to implement their own simulations of spin ice. We begin by tabulating the normalized orientations of spin moments in Tab. A.1. Next we tabulate all sites in hexagonal and cubic coordinates systems of the 36-site unit cell in Tab. A.2 – from which the 12-site and 16-site unit cells can be deduced.

Coordinates	Cubic			Hexagonal		
α	$\frac{\hat{x}}{\sqrt{3}}$	$\frac{\hat{y}}{\sqrt{3}}$	$\frac{\hat{z}}{\sqrt{3}}$	$\frac{2\hat{a}}{3\sqrt{2}}$	$\frac{\sqrt{6}\hat{b}}{3}$	$\frac{\hat{c}}{3}$
1	-1	1	-1	2	0	-1
2	-1	-1	1	-1	-1	-1
3	1	-1	-1	-1	1	-1
4	1	1	1	0	0	3

Table A.1: Tabulated values of spin moment orientations on the pyrochlore lattice given in cubic and hexagonal bases as shown in Fig. **??**.

Coordinates	Cubic			Hexagonal			Present		
Unit Vector	$\frac{\hat{x}}{4}$	$\frac{\hat{y}}{4}$	$\frac{\hat{z}}{4}$	$\frac{\sqrt{3}\hat{a}}{12}$	$\frac{\hat{b}}{4}$	$\frac{\hat{c}}{\sqrt{6}}$	α	12	16
Kagome A	2	1	-1	-5	1	1	3		
	1	2	-1	-5	-1	1	2		
	1	1	0	-2	0	1	1	×	×
	2	-1	1	1	3	1	3		
	1	0	1	1	1	1	2	×	×
	0	1	1	1	-1	1	3	×	×
	-1	2	1	1	-3	1	2		
	1	-1	2	4	2	1	1		
	-1	1	2	4	-2	1	1		
B	3	3	0	-6	0	3	1		×
	3	2	1	-3	1	3	2		×
	2	3	1	-3	-1	3	3	×	×
	3	1	2	0	2	3	1	×	×
	1	3	2	0	-2	3	1		×
	3	0	3	3	3	3	2		×
	2	1	3	3	1	3	3	×	×
	1	2	3	3	-1	3	2		×
	0	3	3	3	-3	3	3		×
C	5	3	2	-4	2	5	1		
	3	5	2	-4	-2	5	1		
	5	2	3	-1	3	5	2	×	
	4	3	3	-1	1	5	3		
	3	4	3	-1	-1	5	2	×	
	2	5	3	-1	-3	5	3		
	3	3	4	2	0	5	1	×	
	3	2	5	5	1	5	2		
	2	3	5	5	-1	5	3		
Triangle A	0	0	0	0	4	0	4		
	-2	2	0	0	0	0	4	×	×
	-2	0	2	6	2	0	4		
B	2	2	0	-4	0	2	4		×
	2	0	2	2	2	2	4	×	×
	0	2	2	2	-2	2	4		×
C	4	2	2	-2	2	4	4	×	
	2	4	2	-2	-2	4	4		
	2	2	4	4	0	4	4		

Table A.2: Positions of spins in the three pyrochlore unit cells used in this work. The basis of the 36-site unite cell is given as integer multiples of vectors along the cubic and hexagonal orthogonal coordinate systems shown in Fig. 3.4. A *present* column is included to indicate the presence of sites shared between the 36-site unit cells and the enclosed 12-site and 16-site unit cells. The α column denotes the FCC sublattice the spins belong to and Tab. A.1 provides the spin moments of each sublattice. The two leftmost columns categorize the spins by their triangular and kagome layers and ABC stacking configuration explained by Fig. **??**.

B

APPENDIX B: IMPLEMENTATION OF EWALD MATRIX

In MC simulations of DSI, dipolar interactions are often the bottleneck of the code, governing the minimum amount of time a simulation requires to finish. The origin of the bottleneck can be distilled to the subject of *cache memory* which is a block of memory in a computer that can be accessed much quicker then other blocks of memory. For the benefit of the reader, we outline an algorithm which exploits the symmetry of crystal structures to create an efficient implementation of calculating dipolar energies. For brevity, the specific proof is not provided, instead a toy problem and To do this we must first establish an indexing with which we will call upon memory locations, a convenient choice for an index γ is given by the *grid* indexing

$$\gamma = (HLb)\,i + (Lb)\,j + (b)\,k + l \tag{B.1}$$

where $\{H, L, b\}$ are obtained by the $[L, H]^b_{\{\text{cube, hex}\}}$ convention established in Sec. 3.2.1, and $\{i, j, k, l\}$ are the number of unit cell translation vectors and basis vector which connect the origin with the point. This indexing scheme lends itself naturally to the spatial periodicity of lattices as shown by a 2D example in Fig. B.1 (a).

Using this indexing scheme any spin b_i can be related to another spin b_0 located in the unit cell containing the origin. Given this symmetry only bN calculations need to be made in the Ewald method and stored during simulation increasing the likelihood of cache hits. To access these symmetry related interactions one only needs to calculate

Listing B.1: C code snippet for optimized calculation of local field updates using the reduced Ewald matrix using a grid index. For clarity we have denoted $\{\texttt{i1} = i, \texttt{i2} = j, \texttt{i3} = k, \texttt{i4} = l, \texttt{s} = 2\sigma_\alpha\}$, and $\texttt{Ewald}$ is the reduced Ewald matrix given by all pairwise Ewald interactions for b spins residing in the unitcell containing the origin.

```c
int j=0;
for (int j1=0; j1<L; j1++){
    d1 = L*(i1-j1 + (j1>i1 ? L:0));
    for (int j2=0; j2<L; j2++){
        d2 = H*(d1 + i2-j2 + (j2>i2 ? L:0));
        for (int j3=0; j3<H; j3++){
            d3 = b*(d2 + i3-j3 + (j3>i3 ? H:0)) + i4;
            for (int j4=0; j4<b; j4++)
                localField[j++] += s*Ewald[d3][j4];
        }
    }
}
```
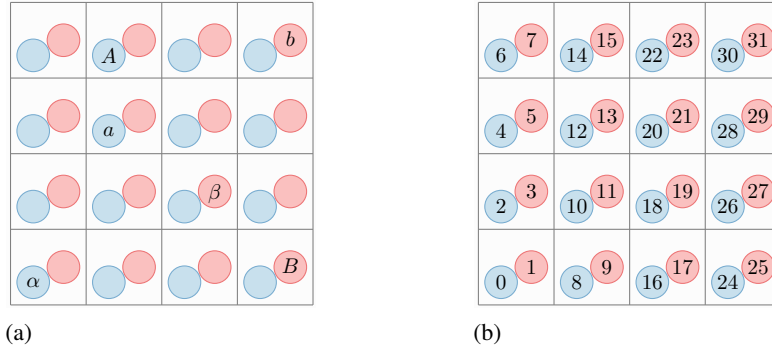
(a)   (b)

Figure B.1: A two dimensional toy example of (a) grid indexing and (b) the symmetry related interactions present. Three interactions are shown: *α-β*, *a-b*, and *A-B*, *each with identical interaction when using PBCs*. An effective way to exploit the symmetry present in the system is to assign a *grid indexing* as shown in (b) which can be used with Lst. B.1 to reduce the interaction Hamiltonian from $\mathcal{O}(L^2)$ to $\mathcal{O}(bL)$, where L is the charecteristic length of the system and b is the number of spins in the basis.

the number of spins between a given spin-pair to access it in the Ewald lookup table of the matrix. Given this property the optimization procedure reduces to performing the index calculation in as minimal moves as possible. Explicitly given a flip of spin α, the change in local fields for all other spins in the system is given by Lst. B.1 A similar procedure follows for the self-energy of the loops necessary for optimization at lower temperatures when the rejection rate approaches unity.

C

APPENDIX C: STACKING OF THE S-STATE

A complete understanding of the S-state requires a discussion of how the meandering majority spins are related with the spins above and below it. This translation vector which we refer to as the *stacking vector* is most easily understood by examining a $[2,2]_\text{cube}$ system as shown in Fig. C.1. As mentioned in Sec. 3.2.1, any $[L,L]_{textrmcube}$ system can be expressed as $2L \times 2L$ kagome lattices with L layers, a $[2,2]_\text{cube}$ is thus the smallest system to study the S-state stacking in cubic and hexagonal systems. Given only two layers exists and the employment of PBCs, the stacking vector between planes must be equivalent to the translational vector of the system, thus

$$v_\text{stack} = 2r_\text{nn} \left(\sqrt{2}\hat{y} \right) \tag{C.1}$$

as shown in Fig. C.1, where r_nn is the nearest neighbour distance.

Applying the appropriate rotations require to bring the $\hat{x}$, $\hat{y}$, $\hat{z}$ basis to the $\hat{a}$, $\hat{b}$, $\hat{c}$ basis defined in Sec. 3.2.1, the stacking vector is

$$v_\text{stack} = \frac{2r_\text{nn}}{\sqrt{3}} \left(\hat{a} + \sqrt{3}\hat{b} + \sqrt{2}\hat{c} \right). \tag{C.2}$$

This stacking vector is significantly more complicated to visualize the cubic stacking vector. An illustration of the non-trivial relation between the stacking vector hexagonal PBCs is provided in Fig. C.2.
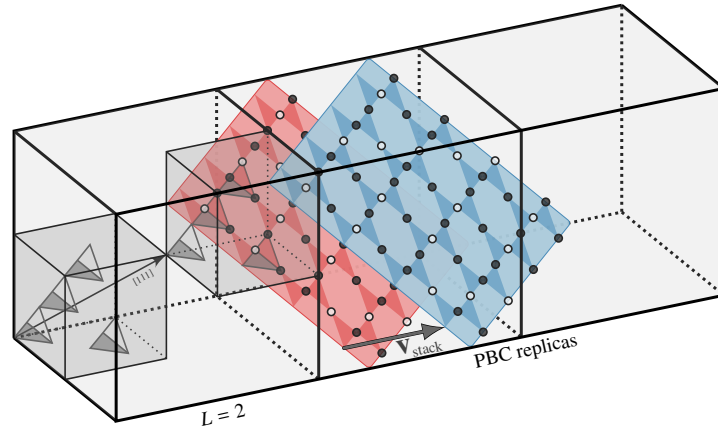

Figure C.1: Stacking of the S-state for a $[2,2]_\text{cube}$ system with separate kagome planes represented in red and blue with the PBCs unwrapped as in Fig. 3.5. Two cubic unit cells are shown related by a thin translational vector along the [111] direction, to help give reference for the direction of the applied field. A thick gray arrow shows the translational stacking vector relating each of kagome plane, while black and white dots respectively show majority and minority spins point along or against the applied magnetic field.
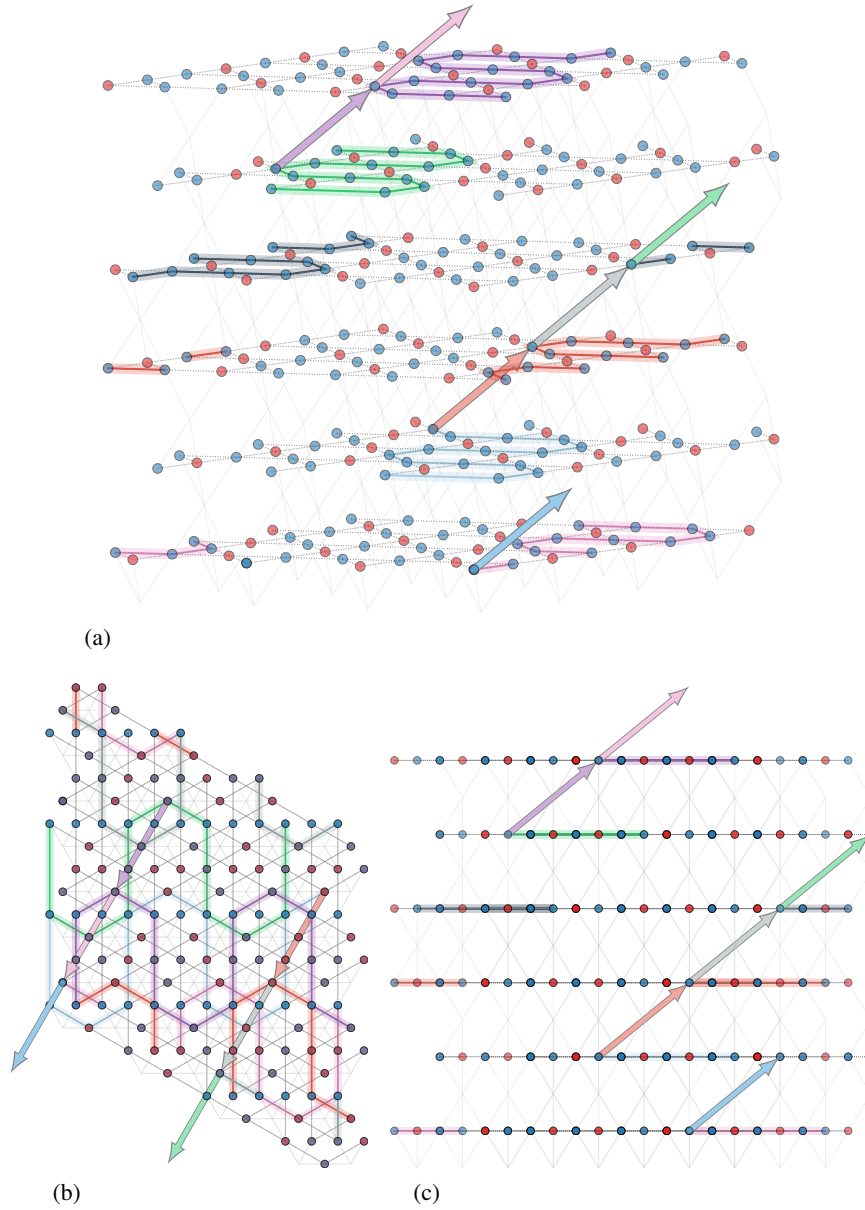
(a)

(b)   (c)

Figure C.2: Stacking of the S-state for a $[4, 2]^{12}_{\mathrm{Hex}}$ system to demonstrate the stacking in a hexagonal coordinate system. Three orientations of the figure are provided to aid the reader in understanding how the stacking vector is commensurate with the system. Red and blue dots indicate majority and minority spins which have been arranged in an S-state configuration. One characteristic meandering line is highlighted for each kagome plane, connected to another kagome plane by a stacking vector v_{stack} of the same colour. Thin gray lines have been added to aid the reader relate the positions of spins and planes with that of the pyrochlore lattice.